MECHANICAL CHARACTERIZATION OF MODULUS-TUNABLE AND SURFACE-MODIFIABLE POLYDIMETHYLSILOXANE WITH AFM

Ye Tian

Thesis Advisors: Prof. Wei Chen

Prof. Katherine Aidala

A thesis presented to the faculty of Mount Holyoke College in partial fulfillment of the requirements for the degree of Bachelor of Arts with honors

December 2014

ACKNOWLEDGEMENT

This research project would not have been possible without the continuous encouragement and genuine support from my research advisor: Prof. Wei Chen. Thank you for accepting me into your lab when I was only a first-year, thank you for reading and revising my weekly reports for the entire three years, and thank you for being such a caring mentor who always gave me the best advice and a hug when I was most vulnerable. Because of your careful guidance, I am now ready to pursue my dream.

To Prof. Kathy Aidala, for being an incredible role model and mentor for me. Thank you for your insightful suggestions for this project during our meetings, and thank you for giving me the freedom to explore the topic of my interest while supporting me when I was faced with difficulties. To Prof. Maria Gomez, thank you for being on my thesis committee and being extremely supportive for my special senior symposium.

To Dr. AnneKathryn Goodman at Mass General Hospital, for being such an inspiring mentor and an incredible surgeon. Because of your unconditional trust and love, I found my passion in medicine. All I wish is to become a caring physician like you.

To my project mentors Wanxin and Alyssa, thank you for being the most amazing and patient peer mentors for me during your time at MHC. To my past and current lab mates: Lan, Mimi, My-Linh, Yen, Lien, Bhanushee,

Tarnuma, Lizzie, Akchheta, Mina, Krishma, Xiaofan; thank you for your company, suggestions, and friendship.

To my friends Yixue, Qinxia, Liye, Mary, Ester, Cis, and Yujia, thank you for being there with me when I needed, thank you for going to library with me and having dinner with me, and thank you for sharing the most precious three and half years of college life with me.

Lastly, I would like to thank my parents and host family. To mom and dad in China, thank you for your unconditional love and support, thank you for believing in me and respecting my choice, and thank you for providing me with this amazing opportunity to study in America. To the Li family in New Jersey, thank you for hosting me during my senior year in high school and treating me as part of the family. I am forever grateful for your help.

TABLE OF CONTENTS

	Page number
CHAPTER 1. INTRODUCTION	
1.1 Project Motivation and Objectives	1
1.2 Polydimethylsiloxane Substrate: Structure and Properties	5
1.3 Substrate Fabrication Reactions: Thiol-ene Click Chemistry and Platinum-Catalyzed Hydrosilylation Reaction	7
1.4 Contact Mechanics Models	13
1.5 Surface Modification: Plasma Oxidation and Collagen Adsorption	18
1.6 Surface Characterization	20
CHAPTER 2. EXPERIMENTAL	
2.1 Materials and Apparati	27
2.2 Methods	29
2.3 Characterization	32
CHAPTER 3. RESULTS AND DISCUSSION	
3.1 Using Thiol-ene Click Chemistry to Design Stiffness-tunable Cross-linked PDMS	35
3.2 AFM Parameter Optimization for Nano-indentation Measurement	48
3.3 Effect of Collagen Adsorption and Plasma Oxidation on Surface Chemical and Mechanical Property of PDMS	57
CHAPTER 4. CONCLUSIONS AND FUTURE DIRECTIONS	77

LIST OF FIGURES AND TABLES

	Page number
Figure 1. Morphologies of tumorigenic breast cancer cell line cultured on (a) commercial polystyrene petri dish; (b) native (10:1) PDMS; (c) plasma-oxidized (10:1) PDMS.	5
Figure 2. Young's modulus of native collagen fibril and cross-linked collagen fibril measured by AFM.	5
Figure 3. Structure of polydimethylsiloxane and the commonly observed bond rotations.	6
Figure 4. Demonstration of a polystyrene bead indenting a sample supported by glass coverslip.	15
Figure 5. Water droplet deposited on solid substrate, forming three-phase contact lines.	20
Figure 6. Acquisition of advancing and receding contact angle.	21
Figure 7. Basic components of atomic force microscopy.	22
Figure 8. Different operating regimes for oscillating AFM mode.	23
Figure 9. The loading (red) and unloading (blue) force curve of a PDMS thin film.	25
Figure 10. Basic components of X-ray photoelectron spectroscopy.	25
Figure 11. Simplified drawing of cross-linked PDMS network using thiol-ene click chemistry.	36
Figure 12. Young's modulus *versus* molecular weight of vinyl terminated PDMS.	38
Figure 13. Young's modulus *versus* [SH]/[vinyl] ratio for V-05 and SMS042.	38
Figure 14. Young's modulus as a function of crosslinker	41

functionality.

Figure 15. Young's modulus as a function of UV irradiation time. Measurement was carried out 3 h after sample fabrication. 45

Figure 16. Young's moduli in hard domain resulted from 1000 s UV curing and soft domain resulted from 200 s UV curing. 46

Figure 17. Aging effect on Young's modulus. The same sample was measured twice using the same AFM tip. The first measurement was done immediately after sample fabrication, whereas the second measurement was done one week after the first measurement. 46

Figure 18. Effects of tip wear out on Young's modulus. Measurement was taken on the same sample using old and new AFM tips one week after sample preparation. 47

Figure 19. Dependence of Young's moduli on photoinitiator concentration. Samples were measured three hours after sample preparation. 47

Figure 20. Average film thickness with standard deviation fitted to power equation y = $10^6 x^{-1.594}$. The fit does not include the first point in the plot. 51

Figure 21. Indentation vs. trigger force for films with different spin coating rate. 52

Figure 22 (a). Young's modulus as a function of indenting velocity measured using 3.5μm beaded-tip and 45μm beaded-tip. 54

Figure 22 (b). Indentation depth generated at different indenting velocity by 3.5 μm beaded-tip and 45 μm beaded-tip. 55

Figure 23 (a). Effect of velocity and trigger force on Young's modulus for V05 thiol-ene system. 55

Figure 23 (b). Effect of velocity and trigger force on indentation for V05 thiol-ene system. 56

Figure 24. Young's modulus of samples with different toluene dilution at different indentation velocities using 1000 nN trigger 60

force.

Figure 25 (a) Advancing contact angle of plasma-oxidized PDMS with various plasma-oxidation time monitored for 24 h post-treatment. 60

Figure 25 (b) Receding contact angle of plasma-oxidized PDMS with various plasma-oxidation time monitored for 24 h post-treatment. 61

Figure 26. Dynamic contact angle of 60 s-plasma-oxidized PDMS monitored over 120 h. 61

Figure 27. Dynamic contact angle of the four different surfaces, in addition to 1 h collagen adsorption on native and oxidized PDMS. 63

Figure 28. Dynamic contact angle of native PDMS and collagen on native PDMS after 24 h adsorption. 63

Figure 29. AFM topography scans of native PDMS (a), oxidized PDMS (b), collagen on native PDMS (c) and collagen on oxidized PDMS (d). The red line was drawn on the screen to obtain further information on height profile of the sample across a specific line, and it was not part of the topography image. 65

Figure 30. AFM topography scans of overnight-dried oxidized PDMS in PBS+collagen (a.b) and oxidized PDMS in PBS (c.d) The white feature on the middle-right of (a) was zoomed in to generate (b); the white feature on the lower-right corner of (c) was zoomed in to generate (d). 66

Figure 31. AFM topography scans of collagen on native PDMS at three randomly selected spots. Height trace (first row), height retrace (second row), phase trace (third row), and phase retrace (fourth row) were all consistent with each other for a given spot. 67

Figure 32 (a). Plots of average values and their standard deviation for Young's modulus for four surfaces of interest. 69

Figure 32 (b). Plots of average values and their standard deviation for Pull-off force for four surfaces of interest. 70

Figure 32 (c). Plots of average values and their standard 70

deviation for indentation depth for four surfaces of interest.

Figure 32 (d). Plots of average values and their standard deviation for adhesion energy for four surfaces of interest. 71

Figure 33. 3D image of HtF after 1st degree flattening. 100 nN trigger force, 14 μm/s indenting velocity, and 45 μm diameter beaded-tip were used for this experiment. The force map were taken at a 90 μm *90 μm area with 32 points *32 lines spacing. 73

Figure 34 (a). Force curve of a beaded-tip hitting a blank spot, i.e. the PDMS substrate. 74

Figure 34 (b). Force curve of a beaded-tip hits a fiber and then falls off. 74

Figure 34 (c). Force curve of a beaded-tip hitting directly on a fiber. 74

Table 1. Young's modulus measured using tensile tests implemented via homemade setup and Instron instrument 39

Table 2. V-05 thiol-ene system hydrophobic recovery after 2 min plasma activation. 58

Table 3. Atomic composition of C1s, O1s, Si2s, and N1s for four surfaces of interest obtained via XPS survey (2 sample spots per data point). *Note: the large standard deviation was due to small sample size. 72

Table 4. Atomic composition of C1s, O1s, Si2s, and N1s for collagen coated native PDMS and its control surfaces obtained via high resolution XPS multiplex (4 sample spots per data point). 72

ABSTRACT

In this study we investigated two polymeric reaction systems to fabricate stiffness-tunable and surface-modifiable polydimethylsiloxane (PDMS), a biomaterial commonly used in microfluidic devices for medical diagnostics and single-cell dynamics study. Using thiol-ene photochemistry, we gained insights about how different reaction variants, such as pre-polymer molecular weight, functional group ratio, and UV exposure time affect the stiffness of the cross-linked network. We compared different techniques for measuring stiffness and realized the advantage of atomic force microscopy (AFM) nano-indentation in characterizing the stiffness of soft, heterogeneous materials such as PDMS. We further applied what we learned from the thiol-ene system to platinum-catalyzed hydrosilylation reaction to study the effects of collagen adsorption on native as well as plasma-oxidized PDMS in terms of the dependence of the AFM-measured mechanical properties on surface chemistry.

Chapter 1. INTRODUCTION

1.1 Project Motivation and Objectives

Cell migration is a coordinated event directed by chemical and mechanical cues. It is important in wound healing, immune system response, and cancer metastasis.[1-3] Many environmental stimuli have been identified and extensively studied in the past few decades. For example, chemotaxis guide cell locomotion in response to gradients of soluble chemicals, whereas haptotaxis shows cell response to gradients of insoluble extracellular matrix (ECM) protein gradients.[4-6] In addition, cells are capable of responding to gravitational potential (geotaxis), electrostatic potential (galvanotaxis), and light intensity (phototaxis).[7-9] Intriguingly, cells also exhibit the property of durotaxis, or the apparent preference for a stiff substrate in response to stiffness gradient.[10] As an emerging field, mechanobiology focuses on investigating how a cell can detect, measure and respond to the rigidity of its substrate and how these processes contribute to its development. The specific property has been described as an active tactile exploration process, during which cells exert forces onto the substrate and then receive and analyze the feedback from substrate deformation to choose a desired direction of migration.[10]

In a migrating cell, the cell extends lamellipodia or filopodia by actin filament polymerization at the leading front, anchoring to extracellular matrix

by transmembrane protein called integrin. Then the cell uses myosin, a family of motor protein, to exert contraction force to drag the cell body forward.[11] Mechanical properties of ECM have been shown to affect cytoskeleton stiffness and strength of integrin-cytoskeleton linkages, thus affecting cell locomotion.[12-13] Experimental design allowing for estimation of traction force revealed that cells spread more on stiffer substrates, are less motile, and have less dynamic focal adhesions compared to softer substrates.[14] Besides affecting cell locomotion, substrate stiffness has been shown to impact stem cell differentiation. Engler *et al.* reported that mesenchymal stem cells on collagen-coated hydrogels were differentiated into neural, muscular, and bone cells on substrates that matched the elastic modulus of these tissues.[15]

Although the importance of substrate stiffness in cell migration and stem cell differentiation has been identified, there are ways to improve the system used to study these interesting cell behaviors. For example, several studies used polyacrylamide gel with varied cross-linking density to design substrate with different stiffness[10,17]. However, the differential swelling ratio of hydrogel in aqueous environment due to different cross-linking density could complicate the system, making it difficult to isolate the stiffness contribution from topography contribution. While a few studies used PDMS, a polymer that does not swell in aqueous environment, the fabrication of PDMS was with commercially available Sylgard 184 kit.[16,19] The disadvantage of using the commercial kit is that accurate manipulation of the substrate

stiffness is hindered because of incomplete knowledge of the additives in the commercial kit. The ***first part of our study*** tries to address these two issues by designing PDMS substrates with different stiffness using two PDMS pre-polymers with known molecular structure through photo-chemistry, thus enabling us to impart spatial control of the hard and soft domains.

The ability to measure Young's modulus is important for quantifying stiffness values of hard and soft domains, thus evaluating the effect of gradient sharpness on cell migration. However, most previous studies obtained Young's modulus by assessing homogeneous bulk PDMS using uniaxial tensile test, and it remains unknown whether the surface modulus stays unchanged when the substrate is coated with collagen to enhance cell attachment.[16, 19] It is critical to study surface modulus not only because it might be different from bulk modulus due to its additional spin coating procedure and protein adsorption during fabrication process, but also because cells on PDMS substrate is more likely to experience the stiffness of the substrate near the surface, making the surface modulus measurement more relevant for the sake of mechanobiology study. The ***second part of our study*** is devoted to mechanical characterization using both tensile test and AFM nano-indentation, with the goal of correlating the bulk and surface stiffness measurements and obtaining reproducible results.

However, the stiffness gradient alone is not the entire story. In order for cells to adhere to and grow on the substrate, ECM proteins such as

collagen, fibronectin, or bovine serum albumin (BSA) need to be deposited onto PDMS to promote cell adhesion. As shown in Figure 1 below, parental breast cancer cells appear to be "balled up" on native PDMS or plasma oxidized PDMS, indicating that uncoated PDMS are not favorable for cell growth.[16] Even though cells spread and grow normally on tissue culture-treated polystyrene dish (Figure 1a), the commercially available petri dish does not serve the purpose of mechanobilogy research in terms of providing substrate with tunable moduli.

Since collagen is the most abundant protein in animal kingdom, coating PDMS with collagen was more common than fibronectin and BSA in studies using microfluidics device made of PDMS. Interestingly, a recent study on mechanical property of single collagen fibril has revealed that dehydrated single collagen fibril has Young's modulus of approximately 5400 kPa, an order of magnitude higher than the PDMS substrate it was deposited on (Figure 2). It triggered our interest to study whether coating PDMS with collagen will affect the PDMS surface's chemical and mechanical property. Thus, the ***final goal of our project*** is to apply the optimized AFM nano-indentation parameters to address the important issues affecting cell migration: how does collagen coating affect the chemical and mechanical properties of the PDMS substrate.

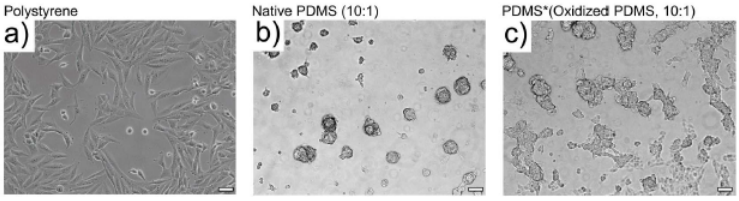

Figure 1. Morphologies of tumorigenic breast cancer cell line cultured on (a) commercial polystyrene petri dish; (b) native (10:1) PDMS; (c) plasma-oxidized (10:1) PDMS.[16]

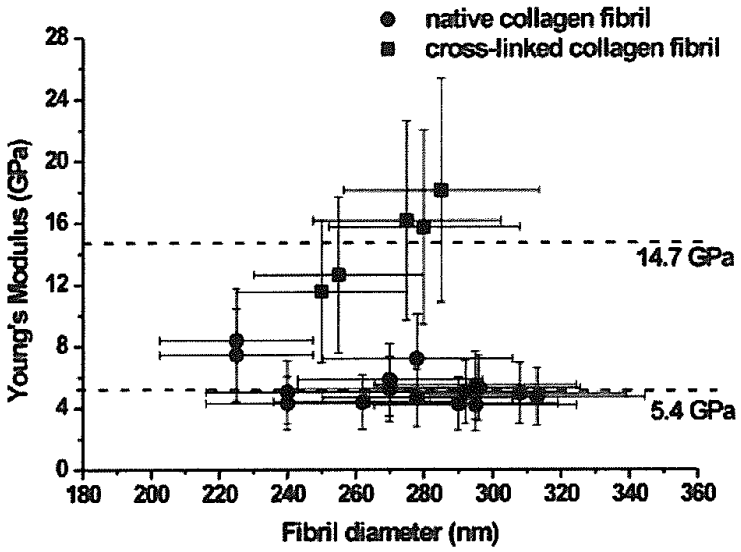

Figure 2. Young's modulus of native collagen fibril and cross-linked collagen fibril measured by AFM.[18]

1.2 Polydimethylsiloxane Substrate: Structure and Properties

Polydimethylsiloxane (PDMS) is the most common organosilicon polymer consisting of alternating silicon and oxygen atoms with two methyl groups attached to each silicon atom.[20] Compared to carbon-carbon backbone, silicon-oxygen backbone has larger bond length and

greater bond angle, resulting in larger spacing of methyl groups and requiring lower energy for rotation and vibration of the molecule.[21]

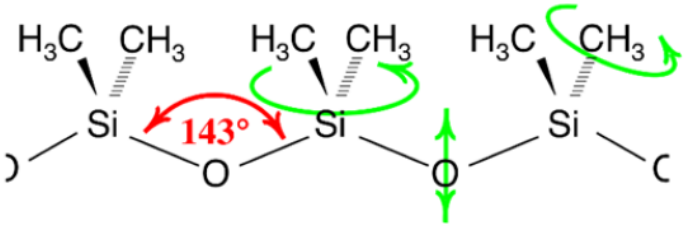

Figure 3. Structure of polydimethylsiloxane and the commonly observed bond rotations.[29]

Silicone materials have been recognized for its biocompatibility in medical applications since 1946, when methylchlorosilanes treated glassware was shown to prevent blood clotting.[22] Biocompatible materials are able to perform in their hosts without causing irritating and sensitizing behaviors.[22] There are two major factors contributing to the biocompatibility of PDMS, the preferred material when it comes to medical applications. First, PDMS has a low level of interaction at their surfaces due to their backbone flexibility, leading to low surface energy and low level of intermolecular interaction. Second, the composition of PDMS polymers are well established; no stabilizers and plasticizers are required because of its intrinsic stability and low T_g.[22]

PDMS is widely used in fabrication of microfluidics device due to its low cost in manufacturing and prototyping, as well as reduced reaction time and complexity compared to the first microfluidic devices using silicon and

glass.[23] The important chemical and physical properties of PDMS make it more than a structural material for microfluidics fabrication.[23] PDMS is optically transparent, allowing for optical detection from 240 nm to 1100 nm. It is electrically and thermally insulating, enabling embedded circuits and can be used to insulate heated solutions. Moreover, it is an elastomer with tunable Young's modulus, which is important for mechanobiology study and allows reversible deformation for microfluidics device fabrication. In addition, it is impermeable to liquid water but permeable to gases and nonpolar organic solvents, allowing it to contain aqueous solution while permitting access of oxygen for living organisms. Lastly, its chemical inertness and nontoxicity provide a suitable environment for chemical or biological assays in microfluidics chambers.[23] Pursuing the objectives of our study will facilitate better understanding of the chemical and mechanical property of this important siloxane.

1.3 Substrate Fabrication Reactions: Thiol-ene Click Chemistry and Platinum-Catalyzed Hydrosilylation Reaction

Thiol-ene click chemistry allows the joint benefits of fast fabrication within seconds and homogeneous system with little interference of oxygen.[24-25] According to Scheme 1, the reaction takes place when UV light excites the photoinitiator to generate a radical, which extracts hydrogen from thiol group to create a thiol radical. The propagation step involves addition of vinyl group

to the thiol radical and transfer of the radical to another thiol group.

Scheme 2 is a more specific reaction mechanism taking place in our study. Darocur 1173 is a type of phenone photoinitiators that generally dissociate into two free radicals upon UV curing. The carbonyl radical is the effective radical because it is very effective in initiating the macromolecular growth, however, the additional radical is not effective and maybe involved in termination.[27] When free radicals are generated, they abstract hydrogen from thiol functional groups to generate sulfur radicals. The reason why initiator-generated radicals first grab hydrogen atoms from thiols rather than reacting with vinyl directly is that sulfur radicals are more stable than carbon centered radicals and thus thermodynamically favorable. In the propagation step, sulfur radicals add to vinyl-ends of pre-polymers, covalently linking the backbone molecule with the cross-linker molecule, generating another radical. It is important to note here that thiol-containing molecules are very strong chain transfer agent, which makes it possible for the regeneration of sulfur radical to react with another vinyl group.[26] Ideally, this reaction can achieve a one to one ratio of thiol and vinyl group reaction thus maximizing the extent of reaction and degree of polymerization.

In classical radical reactions, radicals can either abstract hydrogen atom from –RH bond, or it can react with oxygen to terminate the reaction. A significant advantage of thiol-ene reaction is that oxygen has little or no effect on the radical reaction at room temperature.[25] In addition, it is unlikely in this

system for two radicals to combine and terminate the reaction since the cross-linking points, in the form of radical after hydrogen abstraction, are more likely to react with the electron rich vinyl ends than another radical from another cross-linker due to steric effect.

Scheme 1. General mechanism of thiol-ene reaction in the presence of a photoinitiator and hv.[56]

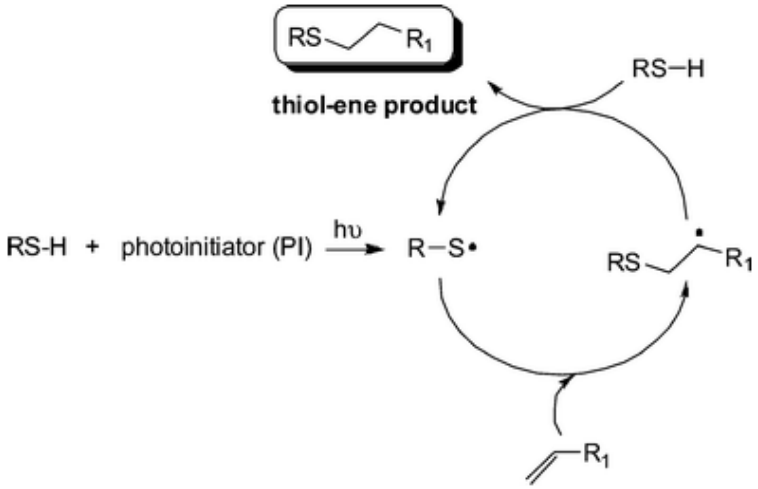

Scheme 2. Reaction mechanism of thiol-ene click chemistry in our study modified from the mechanism depicted in Carlborg *et al*.[25]

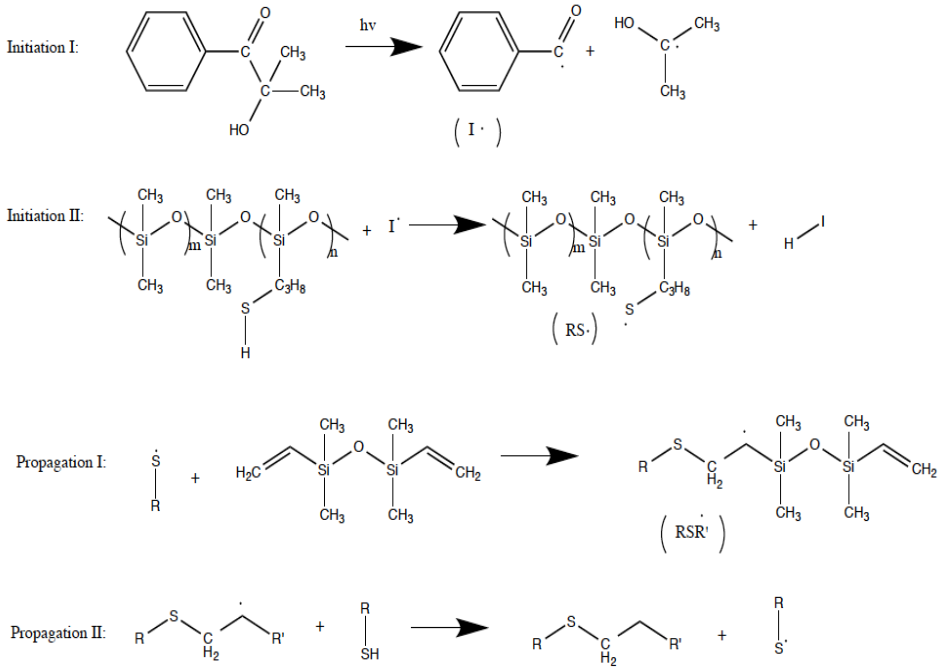

Hydrosilylation reaction is a platinum-catalyzed reaction cross-linking vinyl terminated PDMS and R-SiH (Scheme 3). Platinum complex helps the hydrosilylation reaction to take place by forming multiple unstable bonds with Si-H and vinyl group owing to its empty d orbital, thus making it possible for the migratory insertion and reductive elimination to occur around the complex (Scheme 4).[28] Inhibitory ligands are sometimes added to platinum complexes in order to temporarily control the platinum's ability to catalyze the hydrosilylation reaction. 1-ethynylcyclohexene is an example of an inhibitory ligand due to the fact that the triple bond can more easily bind to platinum center and thus blocking the olefin addition.[28] The first two parts of our study

uses the thiol-ene mechanism because it enables the fabrication of substrate with different stiffness by controlling UV irradiation time for different regions of the substrate. However, due to the quick hydrophobic recovery of thiol-ene cross-linked system after plasma oxidation, the last part of our study uses the hydrosilylation reaction to investigate the effect of plasma oxidation on surface properties.

Scheme 3. A simplified hydrosilylation reaction scheme cross-linking PHMS and V-PDMS with Karstedt's catalyst[29]

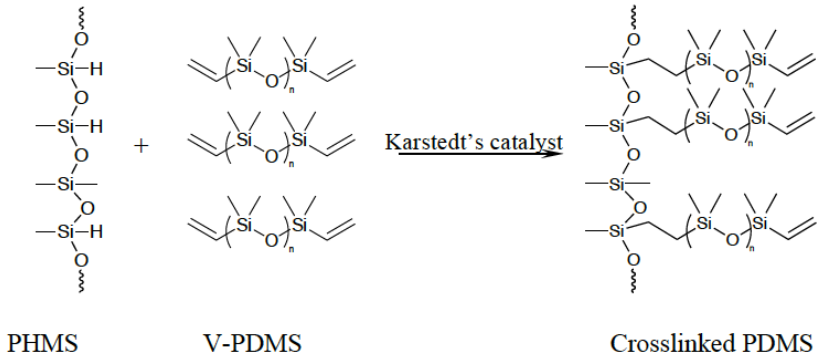

Scheme 4. Catalytic cycle of PDMS hydrosilylation by PHMS based on the Chalk-Harrod mechanism.[28]

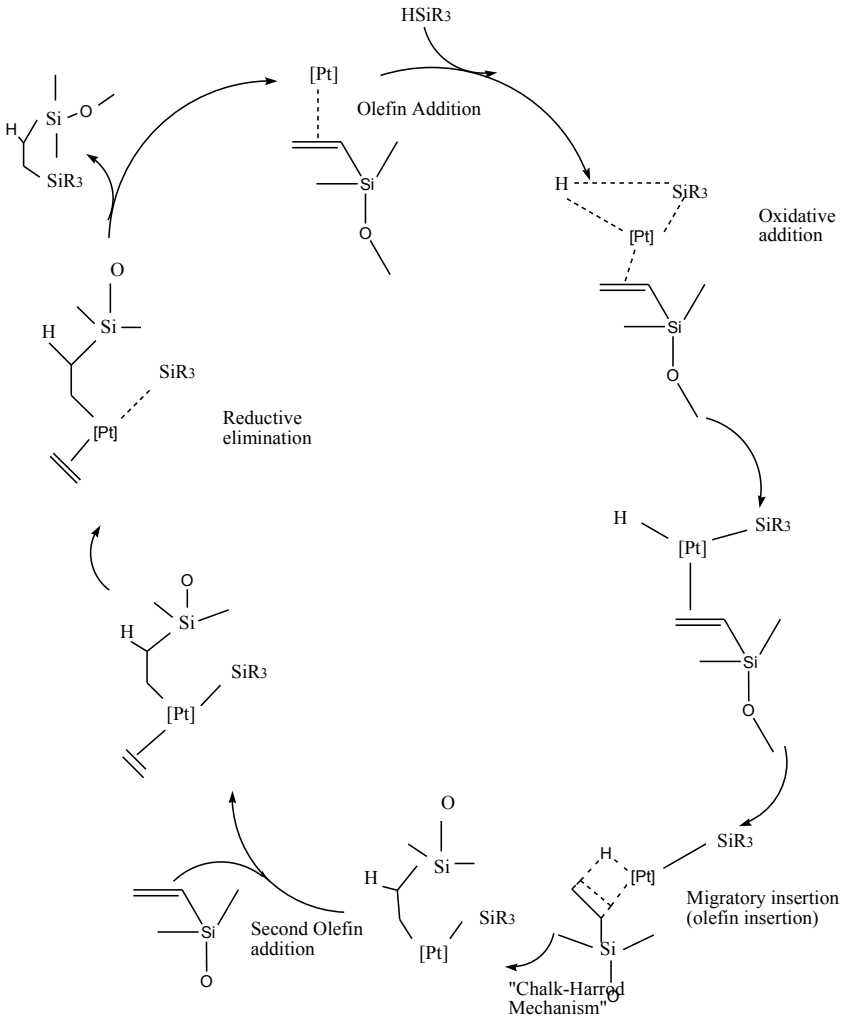

1.4 Contact Mechanics Models

After sample fabrication, we are interested in mechanical characterization of cross-linked PDMS. Mechanical property measurements are of special interests in industrial research because it is the most widely used approach for monitoring rubber materials. Young's modulus, i.e. tensile modulus, is one of the easiest mechanical properties to interpret for rubbers.[30] Young's modulus is the ratio of stress over strain of an elastic material being stretched or compressed.[31] AFM nanoindentation, in combination with an appropriate model, could be used to obtain mechanical property such as Young's modulus. Since Johnson *et al*. first proposed the Johnson-Kendall-Roberts (JKR) model, many studies have shown that JKR model overcomes adhesion problem and that good agreements have been found between modulus obtained from uniaxial tensile test and that from the JKR model.[32-37] In this study, we used tensile test for bulk PDMS Young's modulus measurement, and used AFM nanoindentation for thin-film Young's modulus measurement. The following two subsections introduce how the JKR model is derived from and improved upon the Hertz model.

1.4.1 The Hertz Model

Hertz first studied the contact between two linear, smooth, elastic spheres.[39] He showed that both the size and the shape of the zone of contact are influenced by the elastic deformation of the spheres. This model assumes that there is no adhesion between the two surfaces and that the contact radius

is zero when zero loading force is applied. If two spheres of radii R_1 and R_2 with material elastic constant k_1 and k_2 are pressed together by a loading force P_0, the radius a_0 of surface of contact is given by

$$(a_0)^3 = \frac{3}{4}\pi(k_1 + k_2)\frac{R_1R_2}{R_1+R_2}P_0 \quad (1)$$

Young's modulus is defined by the ratio of normal stress over normal strain when these two terms are linearly proportional. When the strain is small and the deformation is reversible, the relationship between Young's modulus (E), stress (σ) and strain (ε) is described by

$$\mathrm{E} \equiv \frac{\sigma}{\varepsilon} = \frac{F/A_0}{\Delta l/l_0} \quad (2)$$

Where A_0 is the initial cross-sectional area, perpendicular to which a force F is applied. L_0 is the initial length, and Δl is the change in sample length along the direction of applied force.

The relationship between the elastic constant of the material *k* and the Poisson's ratio ν, Young's modulus E is given by

$$k = \frac{1-\upsilon^2}{\pi E} \quad (3)$$

Resulting from local compression, the indentation (δ) is given by

$$\delta^3 = \frac{9}{16}\pi^2(k_1 + k_2)^2\frac{R_1R_2}{R_1+R_2}P_0^2 \quad (4)$$

Defining $R=R_1R_2/(R_1+R_2)$ and $K=4/[3\pi(k_1+k_2)]$, equation (1) can be simplified to

$$(a_0)^3 = RP_0/K \quad (5)$$

The indentation is given by

$$\delta = \frac{a_0^2}{R} \tag{6}$$

Hertz model of two spheres can be extended to a spherical indenter and a linear, elastic half space, which is similar to the scenario applied in AFM nanoindentation, for which a spherical indenter is used to indent the sample material (Figure 4).[33]

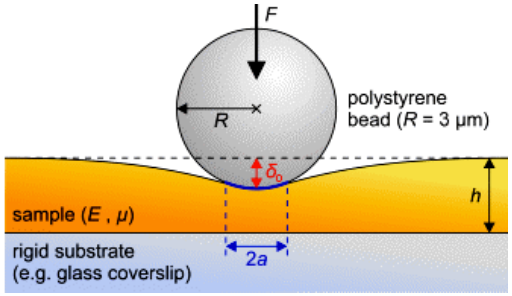

Figure 4. Demonstration of a polystyrene bead indenting a sample supported by glass coverslip.[51]

If the sample material can be viewed as an elastic half space, then its radius is infinitely large compared to indenter radius, thus $R=R_1R_2/(R_1+R_2)$ is simply $R=R_{indenter}$. For a contact radius a_0 that is much smaller than the indenter radius $R_{indenter}$, equation 5 can be written as

$$\delta = \frac{a_0^2}{R_{indenter}} \tag{7}$$

When the indenter's modulus is much greater than the specimen's modulus,

$$k_1 + k_2 = \frac{1-\upsilon_{sample}^2}{\pi E_{sample}} \tag{8}$$

$K=4/[3\pi(k_1+k_2)]$ is simplified to

$$K = \frac{4}{3\pi k_{sample}} \tag{9}$$

Substituting k_{sample} with equation 3, we get

$$K = \frac{4E}{3(1-\upsilon^2)} \tag{10}$$

Thus, equation 5 can be rewritten as

$$P_0 = \frac{4a_0^3 E}{3R(1-\upsilon^2)} \tag{11}$$

1.4.2 The JKR Model

The JKR model modified the Hertz model to account for the significant attractive force in lightly loaded contacts. The new equation shows that even under zero load force, there exists a finite contact area between surfaces, and that it requires an external force that is independent of contact radius to separate the two surfaces.[34] Therefore, the actual force P_1 between the two surfaces need to be calculated through the computation involving the total energy of the system U_T as a function of contact radius, a:

$$\frac{dU_T}{da} = 0 \tag{12}$$

Total energy of the system is the sum of stored elastic energy U_E, mechanical potential energy U_M and surface energy U_S. Since these three energy terms can be written as functions of P_1, the derivative in equation 12 is equivalent to

$$\frac{dU_T}{dP_1} = 0 \tag{13}$$

$R=R_1R_2/(R_1+R_2)$ and $K=4/[3\pi(k_1+k_2)]$. At equilibrium,

$$P_1 = P_0 + 3\gamma\pi R + \sqrt{6\gamma\pi R P_0 + (3\gamma\pi R)^2} \tag{14}$$

$$a^3 = \frac{R}{K}(P_0 + 3\gamma\pi R + \sqrt{\{6\gamma\pi R P_0 + (3\gamma\pi R)^2\}}) \quad (15)$$

in which Υ is work of adhesion between two contacting surfaces per unit of contact area, a is contact radius, P_0 is the loading force, and P_1 is the actual force between two contacting surfaces. When γ=0, we get the Hertz model (eq. 5). When P_0 is zero, we get a finite contact area given by

$$a^3 = \frac{R}{K}(6\gamma\pi R) \quad (16)$$

A pull-off force P_{po} in the opposite direction of the loading force needs to be applied to separate the two surfaces. This P_{po} is calculated by equating the square root in equation 15 to zero in order to get a real solution. Therefore,

$$P_{po} = -\frac{3}{2}\gamma\pi R \quad (17)$$

As shown in equation 17, the pull-off force is only dependent on work of adhesion of the two surfaces, i.e. energy needed to separate the two surfaces. Pull-off force is independent of contact area as well as Young's modulus.

In addition to the JKR model, there are two other models that account for adhesion between two contacting surfaces: the Maugis model and the Derjaguin-Muller-Toporov (DMT) model. To determine which model is more appropriate for a given system, Tabor parameter (μ) as defined is computed:

$$\mu = \left(\frac{R\gamma^2(1-\nu^2)^2}{E^2 z_0^3}\right)^{\frac{1}{3}} \quad (18)$$

where R is tip radius, Υ is work of adhesion per unit of contact area, ν is Poisson's ratio, z_0 is the equilibrium separation of the surfaces in the Lennard

Jones potential and E is Young's modulus. When μ is less than 0.1, the DMT model is selected, when μ is greater than 5, the JKR model applies. Maugis model is appropriate when μ is between 0.1 and 5.[35] Study of the JKR model helps us with the understanding of the data analysis process in calculation of Young's modulus from AFM nanoindentation method.

1.5 Surface Modification: Plasma Oxidation and Collagen Adsorption

Although PDMS has many desirable properties such as optical transparency, gas permeability, and non-toxicity, its innate hydrophobicity has compromised its application in medical devices due to non-specific protein adsorption followed by biofilm formation.[40] Over the past decade, several techniques have been reported to be effective to modify surface hydrophobicity, including surface activation, physical adsorption, and covalent modification.[41] Oxygen plasma belongs to the category of surface activation, which generates reactive species such as electrons, ions, and radicals to attack siloxane backbone to form silanol functional surface structure. The major drawback of surface activation is the fast hydrophobic recovery, a phenomenon describing the oxidized surface regaining its hydrophobicity within hours after plasma treatment.[42] In this study, in addition to fabricating a PDMS surface with slow hydrophobic recovery rate, we are curious whether hydrophilizing the surface is going to have an effect on the

surface mechanical property, i.e., Young's modulus measured by AFM nanoindentation.

Surface modification via physical adsorption has the advantage of simplicity and efficiency compared to covalent modification or surface activation. Common examples of physical adsorption include blocking proteins, nonionic surfactants, charged polymers and polyelectrolyte multilayer.[41] These macromolecules could be adsorbed onto microfluidics channel through non-covalent bonding such as hydrophobic or electrostatic interactions. Conventional blocking proteins such as type-I collagen, fibronectin, and bovine serum albumin (BSA) are the most commonly used model proteins for *in vitro* biological studies to improve cellular adhesion to substrates.[43] Collagen accounts for one quarter of the protein in human body, and it is the major structural protein in connective tissue to form web-like sheets that could be found in tendons, bones, and even the surrounding structures of internal organs. In this project, we are not only interested in evaluating the effect of collagen adsorption on surface hydrophobicity of PDMS, but also interested in exploring its effect on surface mechanical property.

1.6 Surface Characterization

1.6.1 Contact Angle Goniometry

In 1804, Dr. Thomas Young first proposed the well-known Young's equation (eq. 19) to predict the equilibrium contact angle for a liquid in contact with its vapor and a solid at a three-phase contact line.[44]

$$\gamma_{S/V} = \gamma_{S/L} + \gamma_{L/V} \cos\theta \tag{10}$$

in which $\gamma_{S/V}$ is the solid-vapor interfacial energy, $\gamma_{S/L}$ is the solid-liquid interfacial energy, and $\gamma_{L/V}$ is the liquid-vapor interfacial energy; θ is the equilibrium contact angle of liquid droplet on solid surface (Figure 5).

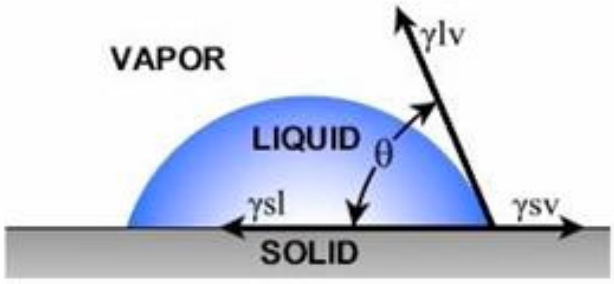

Figure 5. Water droplet deposited on solid substrate, forming three-phase contact lines.[52]

In practice, the observed contact angle is not equal to the theoretical contact angle due to the fact that the wetting phenomenon is more than a static state. In this project, we measure dynamic, advancing and receding, contact angles when the three-phase contact line is in motion using contact angle goniometry. The advancing contact angle (θ_A) characterizes surface hydrophobicity, and it gives the maximum value that the static contact angle

can have on the surface. The receding contact angle (θ_r) characterizes surface hydrophilicity, and it gives the minimum value that the static contact angle can have on the surface (Figure 6). The difference between the advancing and receding contact angles is called the hysteresis, which arises from surface roughness and/or chemical heterogeneity.[45]

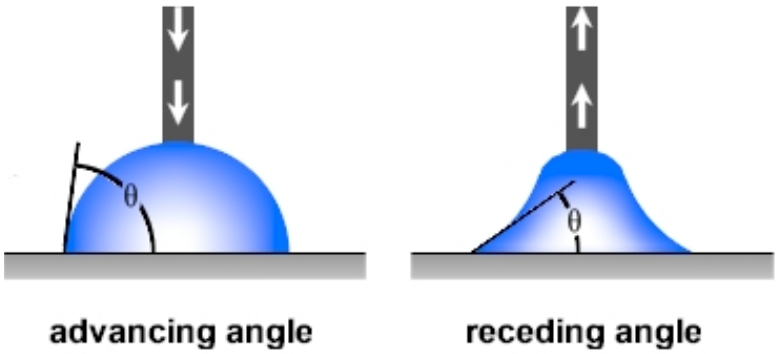

Figure 6. Acquisition of advancing and receding contact angle.[53]

1.6.2 Atomic Force Microscopy

The three most important elements of AFM are piezoelectric transducers, force transducers and feedback control. Piezoelectric transducer is often made of synthetic ceramic materials, and they experience geometry change when electrical potential is applied. The x, y, and z piezoelectrics control the movement of the tip in respective directions. The force transducer measures the force between the probe and the surface. It is an optical lever that consists of a photo detector, cantilever with its integrated probe, and a laser beam (Figure 7). When the cantilever bends relative to the surface, the

optical lever magnifies the small displacement of the probe on the photo detector. The feedback control obtains signal from force transducer and uses it to control piezoelectric transducer in order to keep the set point. When the measured amplitude is greater than set point, z piezoelectric will expand to reach the set point; on the other hand, if the measured amplitude is smaller than set point, then z piezoelectric will decrease to maintain the set point.[38]

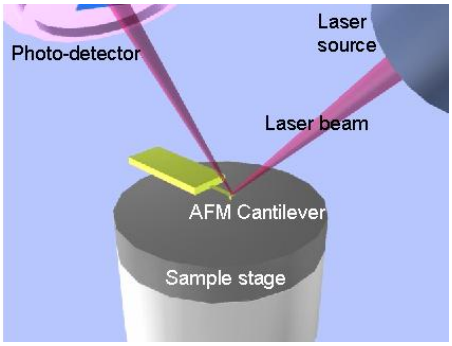

Figure 7. Basic components of atomic force microscopy.[54]

AFM was originally designed to measure topography of the sample. The first available topographic mode was the contact mode, in which the tip is dragged across the sample with the set point maintained at repulsive regime between tip and sample (Figure 8). One disadvantage of using contact mode for topography measurement is that it damages both the sample and the tip. In this mode, the deflection image is the error signal since it measures how much the cantilever is deflected before z piezoelectric adjusts its geometry to return to the set point. Then oscillating mode is invented and well accepted as the topographic mode because it requires small probe-sample force. There are two

modes in the oscillating mode. One is called non-contact AFM, for which the probe stays in the attractive regime of the tip-sample interaction curve (Figure 8). Another is more commonly used intermittent contact AFM (also called AC-AFM or tapping), for which the probe goes through the zero force to attractive force and to repulsive force then come back. AC-AFM is more widely used because it assures that the tip-sample interaction is in the repulsive regime but it is not dragging across the surface. The tip will always be able to pass through the contamination layer of the sample exposed in air and measure the real topography of the surface. In oscillating mode, the amplitude image is the error signal because it records where the feedback control has not been able to correct the z piezoelectric to make up for the sample topography.[38] In this study, we use the AC-AFM mode to measure the surface roughness of cross-linked PDMS.

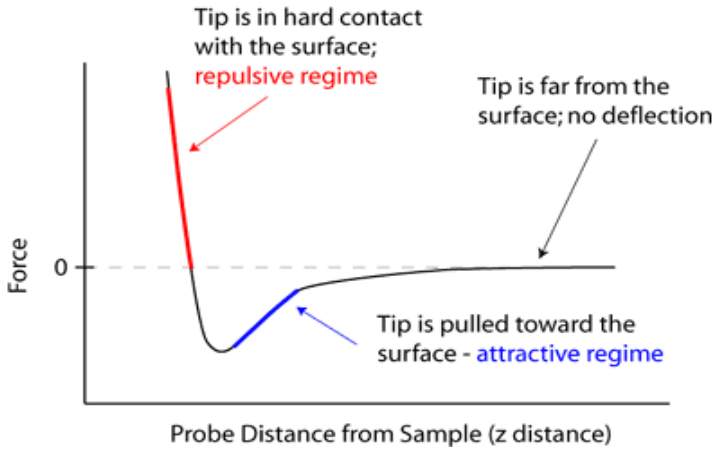

Figure 8. Different operating regimes for oscillating AFM mode.

Other non-topographic modes include force spectroscopy, nanoindentation, electric force microscopy (EMF), magnetic force microscopy (MFM), etc. Force spectroscopy measures the force in between probe and contacting surface; it can indicate the interactive force between two different materials if two different molecules are attached to the probe surface and the sample surface. Nanoindentation records the data as the probe contacts the surface and indents into the sample. EMF and MFM map electric field and magnetic field gradient distribution above the sample surfaces, respectively.

In our study, Young's moduli of thin films were measured by AFM using nanoindentation by taking multiple force curves with forcemap function. The force curve (Figure 9) depicts the process of the tip approaching the surface (red curve), jumping into contact, indenting the substrate, and withdrawing from the sample (blue curve).[35] For nano-mechanical analysis, we adopted the JKR based two-point method proposed by Walker and co-workers.[32] Two points analyzed were both on the unloading curve (blue curve), with one being the lowest point and the other being the intersection between zero force load and the unloading force curve itself. The JKR model takes into consideration the adhesion force between the probe and the surface for soft materials, and the fact that the contact area is larger than Hertz estimation because of larger adhesion energy.

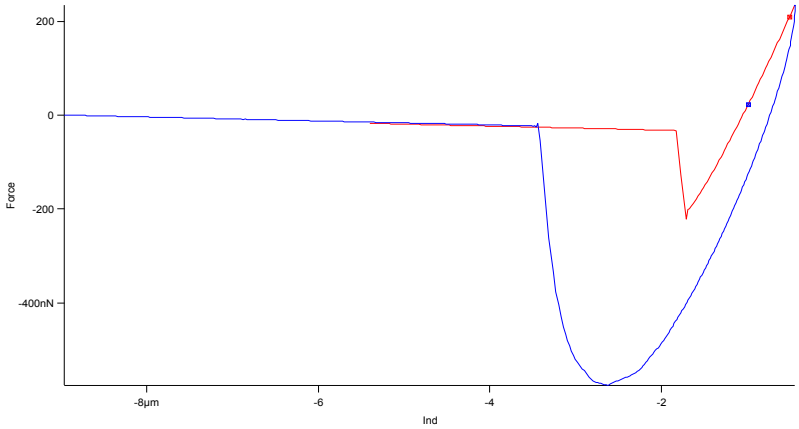

Figure 9. The loading (red) and unloading (blue) force curve of a PDMS thin film.

1.6.3 X-ray Photoelectron Spectroscopy

In 1957, Siegbahn and colleagues generated the first high-quality X-ray photoelectron spectra in Uppsala, applying the principles of X-ray photoelectron spectroscopy (XPS) to chemical analysis.[46] XPS studies the energy distribution of electrons emitted from X-ray-irradiated samples, after which the remaining kinetic energy of the electrons is collected by the electron energy analyzer (Figure 10).

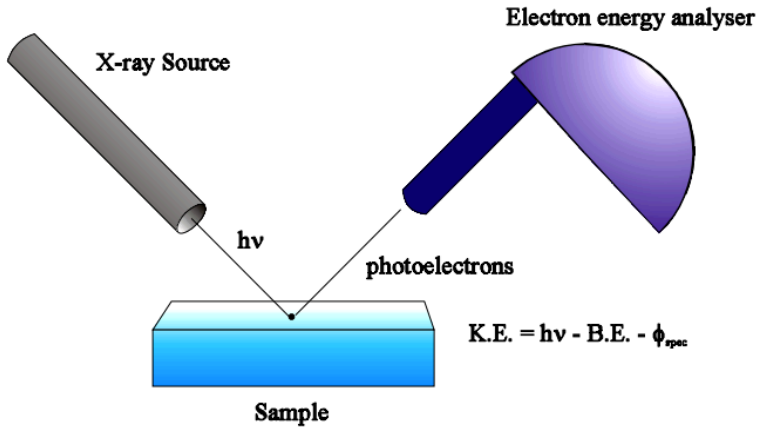

Figure 10. Basic components of X-ray photoelectron spectroscopy.[55]

Because of the conservation of energy, photoelectric effect can be described by

$$E_{h\nu} = E_k + E_\Phi + E_{B(i)} \quad (19)$$

Where $E_{h\nu}$ is the X-ray energy, E_k is the kinetic energy of emitted electron, E_Φ is work function, and $E_{B(i)}$ is the electron binding energy of the *i*th level. By scanning the E_k values of discrete photo lines using an electron energy analyzer, $E_{B(i)}$ could be calculated assuming that E_Φ is constant and known for a particular instrument.[46] It is important to note that the electron binding energy of an atom is a function of its chemical environment, therefore, chemical shift is observed for the same atom in different bonding environment. This special feature makes it possible for XPS to be used for structure determination and study of chemical binding. In our study, we used XPS to study atomic composition of different surfaces of interest.

Chapter 2. EXPERIMENTAL

2.1 Materials and Apparati

General. Silicon wafers (100 orientation, P/B doped, resistivity 1–10 Ω-cm, thickness 475–575 μm) were purchased from International Wafer Service, Inc. Vinyl terminated PDMS (DMS-V05: 800 g/mol, DMS-V21: 6 k g/mol, DMS-V22: 9.5 k g/mol, DMS-V31: 28 k g/mol), mercaptopropylmethylsiloxane dimethylsiloxane copolymer (SMS042 containing 4~6 mol% thiol, 9k g/mol), polymethylhydrosiloxane (HMS-991, 1.4 k-2 k g/mol) and Karstedt's catalyst, or platinum-divinyltetramethyldisiloxane complex, were purchased from Gelest, Inc. Photoinitiator 2-hydroxy-2-methyl-1-phenyl-propan-1-one (Darocur 1173 Ciba®) was generously provided by Ciba Specialty Chemicals. Four-compartment polystyrene petri dish with 100 mm outer diameter and 15 mm height was purchased from Fisher Scientific, Inc. Karstedt's catalyst was further diluted in anhydrous toluene to a final concentration of 5×10^{-5} g/mL and stored at -20 °C. Type I collagen was purchased from Sigma-Aldrich, Inc. It was diluted with 0.1 M acetic acid to reach a concentration of 1×10^{-3} g/mL as a stock solution, which was stored at 4°C. Phosphate buffer saline (PBS) were made by dissolving one PBS tablet (Sigma-Aldrich, Inc.) in 200 mL Milli-Q water purified using Millipore Milli-Q Biocell System (Millipore Corp.) and stored at 4°C.

Instrumentation. Silicon wafers and cross-linked PDMS substrates were oxidized using a Harrick plasma cleaner PDC-001 (Harrick Scientific Products, Inc.). Spin casting was completed using a Laurell WS-400B-6NPP/LITE single wafer spin processor (Laurell Technologies Corp.). Ultra-violet light irradiation for thiol-ene reaction was completed using a UV collimated light source Model 30, along with a constant intensity controller, and a model 150 shutter timer (OAI Inc., CA). The UV light source output spectrum ranged from 300 to 500 nm with peaks at 365, 410, and 440 nm, and the output power was fixed at 22 mW/cm^2. Hydrosilylation reaction occurred in Precision 51221126 Gravity Convection Lab Oven (Themo Fisher Scientific, Inc.). Dynamic contact angles were measured with a NRL C.A. 100-00 goniometer (Ramé-Hart Instrument Co.) connected to an automated imaging system (p/n 100-12-F4-00-UPG). The Gilmont syringe (Gilmont Instrument Co.) was attached to a 24-gauge flat-tipped needle. Thermo NESLAB heated baths (Thermo Fisher Scientific, Inc.) were used for collagen adsorption. Atomic composition of PDMS thin-films was measured by Quantum 2000 X-ray photoelectron spectroscopy (Physical Electronics, Inc.) and analyzed using Multipak Version 6.1A. The thickness of PDMS thin-films generated using different spin coating rate was measured by a Dektak 150 profilometer (Veeco, Inc.).

Force curve and topography measurements were carried out using MFP-3D AFM (Asylum Research, Inc.) with three different types of tips.

AC160TS-R3 (Silicon lever with Al coating, Silicon tip without coating, 9±2 nm diameter, 300 kHz, 26 N/m) were used for topography scan (Asylum Research, Inc.). CP-FM-SiO-B-5 manufactured by NanoAndMore (NanoAndMore, Inc.) (3.5 μm diameter, SiO_2 colloidal particle attached Silicon cantilever, 45-115 kHz, 0.5-9.5 N/m) and specially designed tip purchased from Novascan (Novascan Technologies, Inc.) (45 μm diameter polystyrene colloidal particle attached Silicon cantilever, 8.9 N/m) were used for AFM nanoindentation. AFM data processing and analysis were carried out using Igor Pro 6 (WaveMetrics, Inc.).

2.2 Methods

2.2.1 Preparation of Silicon Wafers

Silicon wafers were cut into 1.3 cm × 1.3 cm, rinsed with distilled water, and dried with compressed air. The wafers were then placed in a 110 °C oven for 30 min, and plasma oxidized for 15 min under high power.

2.2.2 Preparation of Cross-linked PDMS Substrate via Thiol-ene Reaction

Photocross-linking reaction between vinyl-terminated polydimethylsiloxane (V-PDMS) and mercaptopropylmethylsiloxane dimethylsiloxane copolymer (SMS) in the presence of photoinitiator Darocur 1173 occurred upon UV-irradiation. Samples were prepared using V-PDMS of various molecular weights, as well as different functional group ratios of

SMS and V-PDMS ([SH]: [Vinyl]) for a fixed V-PDMS molecular weight (DMS-V05). Cross-linked PDMS samples were either prepared as thick samples (0.2 cm) for tensile test measurement or as thin films (6 μm) for all other surface characterization studies.

To prepare a pre-polymer mixture, 0.55 g of vinyl terminated polydimethylsiloxane (V-05, MW 800 g/mol) was added to a scintillation vial, followed by 30 μL Darocur 1173 (1 wt%). The mixture was vortexed for 20 s to ensure sufficient mixing. Then 2.56 g SMS042 was added to the mixture, and the new mixture was vortexed again for 20 s. The mixture was then stored in a lightproof box for 5 min to degas while preventing the polymerization from happening. Thick PDMS samples were prepared by pouring the mixture from glass vial into one compartment of the polystyrene petri dish. The petri dish was then placed under UV light and irradiated for 999 s.

PDMS thin films supported on silicon wafers were prepared by spin-casting pre-polymer mixture onto pre-cut silicon wafers followed by UV exposure. 100 μL of mixture was withdrawn from the scintillation vial using a micropipette and gently transferred to the top of a 1.3 × 1.3 cm silicon wafer. Spin coating parameters were optimized at 2000 rpm for 30 s. The spin-coated sample was then transferred to the top of a PET film placed under the UV lamp and irradiated for 999 s.

2.2.3 Preparation of Cross-linked PDMS Substrates via Hydrosilylation Reaction

Cross-linked PDMS was prepared by diluting 2.8 g of PDMS-V31 with 0.7 g toluene in a scintillation vial. The solution was then mixed with 0.067 g of PHMS-991 (75 μL) prior to adding 150 μL of diluted Karstedt's catalyst. Each addition was followed by 20 s of high-speed vortexing to ensure sufficient mixing. The mixture was spin casted onto plasma-oxidized silicon wafers as soon as the bubbles created by vortexing disappeared. A micropipette was used to dispense 100 μL of mixture onto each silicon wafer and spun at 2000 rpm for 30 s. Following spin casting, samples were cured in a 100 °C oven for 1.5 h. To study the effect of surface modification on surface mechanical property, cross-linked PDMS samples were modified via plasma oxidation and/or collage adsorption. Plasma oxidation time was optimized for 1 min at high power, while collagen adsorption was carried out at 37 °C for 24 hours.

2.2.4 Adsorption of Collagen onto PDMS Thin Film

Collagen stock solution (0.1 % in 0.1 N acetic acid solution) was prepared by stirring 0.01 g of collagen in 10 mL 0.1 N acetic acid at room temperature in a scintillation vial. It took at least 30 min for collagen to dissolve. For each adsorption experiment, the stock solution was diluted with PBS to reach a final concentration of 30 μg/mL. Samples were loaded in

wafer holder and placed in a Schlenk tube, followed by careful pouring of collagen solution into the tube along the side. The immersed samples were left in 37 °C water bath for 24 h to achieve sufficient collagen adsorption. After 24 h, the solution was diluted with PBS three times before transferred to a beaker of Milli-Q water. Samples were then rinsed with Milli-Q water three times from the squirt bottle and dried in a desiccator overnight before further characterization.

2.3 Characterization

2.3.1 Determination of Young's Modulus of PDMS Thick Sample Using Tensile Test

Each cross-linked PDMS thick sample was cut into a dog-bone shape using a pre-made copper cutter following the ASTMD638 standard (dimension: 0.80 cm width * 2.00 cm length). The original length of the middle portion of the dog-bone was defined by the experimenter using two thin-lines on the side of the dog-bone shaped sample. The cross-sectional area and the original length between the two lines drawn on the side of the middle portion of the dog-bone were measured with a caliper. Incremental weight (10 g to 150 g) was added to elongate the gel vertically while photos were taken each time the weight changes. ImageJ was used to measure the change in sample length during the process and Young's modulus was calculated by the

ratio of tensile stress over tensile strain in the linear region (eq. 2), with the strain limited to 5~30 %

2.3.2 Surface Characterization: Atomic Force Microscopy

Contact mode AFM was applied to extract Young's moduli of PDMS thin films. Beaded-tip (45 μm in diameter) was calibrated at the beginning of each experiment to correlate cantilever deflection to voltage applied to piezoelectric, and obtain basic information about the tip such as its spring constant. Other quantitative parameters such as sum, deflection, lateral were also recorded at the beginning of each experiment. After calibration, a sample was mounted onto a glass slide and force maps (4 lines * 5 points) were obtained at five randomly selected 20 × 20 μm square area for each selected trigger force (100 nN and 1 μN). Standard deviation was calculated using data extracted from 100 force curves obtained from AFM nanoindentation. Force distance was optimized to 3.49 μm and velocity was 14.07 μm/s.

AC mode AFM was applied to scan the topography of PDMS thin films. AC160TS tip was auto tuned at -5% before 20 × 20 μm scan and 1 × 1 μm scans were taken. RMS roughness was recorded after necessary masking and flattening of images.

2.3.3 Surface Characterization: Contact Angle Goniometry

Advancing and receding contact angles were taken at three random spots on each sample and averaged. At each spot, a total of 10 measurements were taken during the advancing or receding process at an interval of 0.5 s. Advancing contact angle was chosen when the angles stopped increasing further when more water is being deposited onto the surface, while receding contact angle was chosen when the angles stopped decreasing further when more water is being withdrawn into the syringe. Contact angle measurements were used for optimizing the plasma oxidation time, monitoring hydrophobic recovery, as well as for characterizing the hydrophobicity of the four different surfaces: native PDMS, oxidized PDMS, collagen adsorbed on native PDMS, and collagen adsorbed on oxidized PDMS.

2.3.4 Surface Characterization: X-ray Photoelectron Spectroscopy

XPS survey spectra were obtained on all four types of surfaces mentioned above to assess the extent of change in atomic composition due to surface modification. Two samples of each surface type were loaded onto the sample stage, and two spots (200 μm in diameter) were randomly chosen on each sample. Al-Kα x-ray source was directed to the sample, and atomic compositions of C, O Si, N were detected at 45° take-off angle. XPS multiplex spectra in high resolution were obtained only on native PDMS and collagen-coated native PDMS. Acquisition time was chosen so that high enough resolution spectra were obtained without causing surface damage.

Chapter 3. RESULTS AND DISCUSSION

3.1 Using Thiol-ene Click Chemistry to Design Stiffness-tunable Cross-linked PDMS

Overview In previous studies carried out by our group, researchers have identified parameters contributing to mechanical tunability of cross-linked PDMS using the hydrosilylation system, such as molecular weight of pre-polymer and functional group ratio.[29] Here, we adapt and modify those parameters to the thiol-ene system and explore how these factors affect the mechanical tunability of cross-linked PDMS in the new system. We expect several factors to contribute to the cross-linking density of the system, including molecular weight of vinyl-terminated PDMS, functional group ratio between thiol and vinyl group, UV irradiation time, and photoinitiator concentration.

3.1.1 Young's Modulus of Bulk PDMS Measured by Tensile Test

Figure 11 is a simplified drawing of the cross-linked PDMS network consisting of V-PDMS and SMS042. In the case of V-05, the moleuclar weight of PDMS backbone is smaller than that of thiol-containing cross-linker.

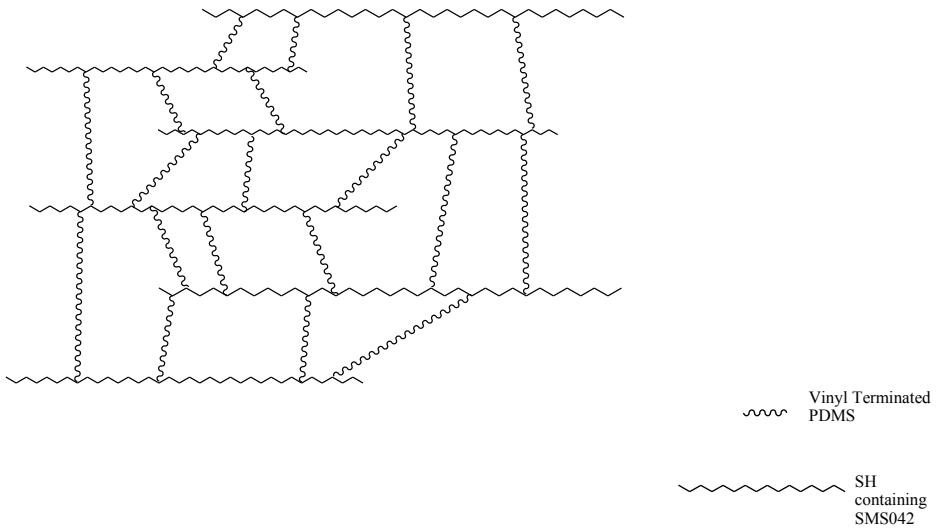

Figure 11. Simplified drawing of cross-linked PDMS network using thiol-ene click chemistry.

Since the stiffness of the cross-linked network is determined by the cross-linking density, it is reasonable to hypothesize that there will be an optimal value for molecular weight and functional group ratio at which the cross-linking density is the highest, resulting in the highest Young's modulus. It is important to find the highest Young's modulus for a certain system, because that value defines the higher end of the range, within which other modulus values could be reached by manipulating the functional group ratio.

According to the tensile test results, Young's modulus was dependent on molecular weight of vinyl terminated PDMS (Figure 12) and [SH]/[vinyl] functional group ratio (Figure 13). Figure 12 showed that Young's modulus decreased as molecular weight of V-PDMS increased as the general trend. One reasonable explanation for the trend was that it was easier for the lower MW V-PDMS to diffuse in the mixture and more likely to reach a sulfur

radical to form a cross-link. The higher MW vinyl-terminated PDMS also has higher viscosity, and high viscosity in bulk polymerization could lead to low conversion.[26] Furthermore, lower molecular weight PDMS backbone resulted in higher cross-linking density because the chains were closer together, therefore the cross-linking density was expected to be higher.

Vinyl terminated PDMS V-05 was chosen to be further studied because it gave a greater range of Young's modulus values to manipulate by varying functional group ratio, UV irradiation time, and photoinitiator concentration. The trend shown in Figure 13 supported our hypothesis that there would be an optimal functional group ratio at which Young's modulus reaches a maximum value for a given molecular weight V-PDMS. We attribute the trend to different cross-linking density and steric effect. The average number of thiol groups on each SMS042 molecule was 6, and that the maximum modulus was obtained when r = 1.2 (r = [SH]/[vinyl]=6/5), which meant that on average, every six thiol groups reacted with five vinyl group. The reason why r=1 did not give the highest modulus was that even though in theory r=1 would enable every –SH to react with a vinyl group, the polymers were present as random coils and that steric effect made it less likely for all six -SH to be available for thiol-vinyl reaction. When r value was less than 1.2, not all of the vinyl groups were incorporated into the PDMS network, so it affected the homogeneity of the system and decreases the Young's modulus. When r value was greater than 1.2, the excess –SH groups decreased the

cross-linking density and thus decreased the Young's modulus. Lastly, the optimal ratio was chosen to compare the homemade tensile test method with the Instron instrument for PDMS thick samples. Instron is a material testing machine for tensile test commonly used in engineering. We demonstrated that the two methods could give comparable results (Table 1) and thus the general trend obtained using homemade setup was reliable and meaningful.

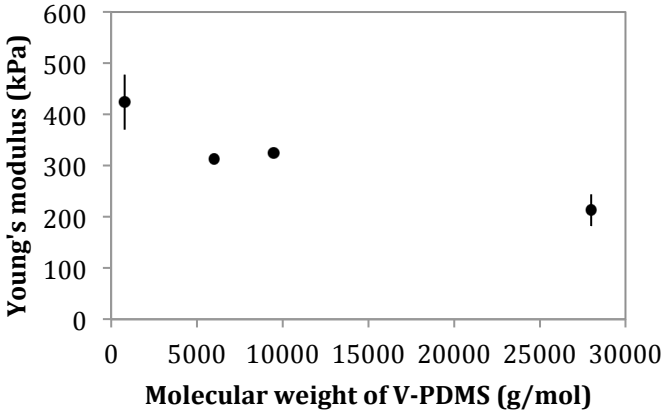

Figure 12. Young's modulus *versus* molecular weight of vinyl terminated PDMS.

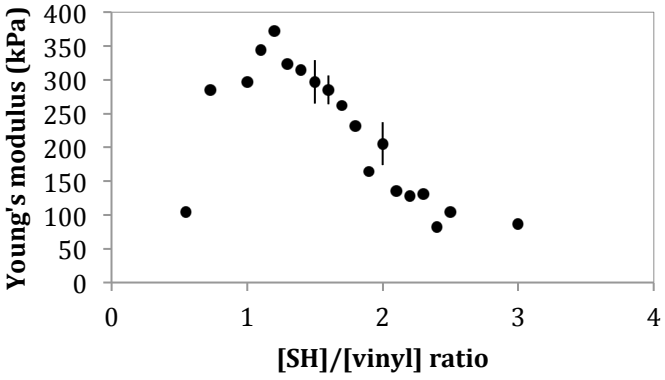

Figure 13. Young's modulus *versus* [SH]/[vinyl] ratio for V-05 and SMS042.

Table 1. Young's modulus measured using tensile tests implemented via homemade setup and Instron instrument

	Home-made tensile test	Instron tensile test
Young's modulus (kPa)	424±51	476±25

Larsen *et al*. summarized previous studies comparing experimental values of elastic modulus of PDMS-PHMS system with theoretical models.[47] In that specific system, methylhydrosiloxane-dimethylsiloxane copolymer (HMS) was the cross-linker while vinyl terminated PDMS was the backbone. The molecular weight of the backbone was much greater than that of the cross-linker, therefore the factors contributing to network elasticity were simplified to the functionality of cross-linker and the molecular weight of PDMS backbone. There are mainly three models describing the correlation between elastic modulus and concentration of elastically effective chains: the affine, phantom, and junction affine network models.[48] The fundamental difference between these three models is the fluctuation of cross-links. The phantom model (eq. 21) assumes that deformation of the network strand is suppressed by fluctuation of cross-links because cross-links fluctuate. Whereas the affine model (eq. 22) assumes that cross-links do not fluctuate thus the strands deform in the same manner with the macroscopic deformation. In addition, the phantom model accounts for the effects of cross-linker functionality on elastic modulus, while the affine model does not.[47] The

junction affine model is the intermediate model between these two extremes.[48] The network is predicted to be more phantom-like at larger deformations and more affine-like at small deformations.[47] When cross-linker functionality is very large, phantom equation coincide with the affine equation.

$$E_{ph} = \left(1 - \frac{2}{f}\right)\frac{\rho}{M}RT \quad (21)$$

$$E_{af} = \frac{\rho}{M}RT \quad (22)$$

where E is Young's modulus, f is functionality and is equal to 6/r, ρ is the density of PDMS, M is the molecular weight between cross-linkers, R is gas constant, and T is temperature in Kelvin.

As illustrated in Figure 11, our PDMS-SMS042 system is quite different from PDMS-PHMS system in that the molecular weight of cross-linker is not negligible compared to the molecular weight of PDMS backbone. This makes it less convincing to simplify molecular weight in between cross-linker to molecular weight of V-PDMS. Instead, we proposed to relate M to molecular weight of SMS042 and functionality by the following equation

$$M = M_o/f \quad (23)$$

in which M_o is the molecular weight of cross-linker SMS-042. The physically meaningful range of f is between 2 to 5 for SMS-042 for two reasons. First, the functionality has to be greater than 2 so that the cross-linker will be able to connect two other pre-polymers together. Second, for SMS-042 the maximum

functionality is 5, which corresponds to the calculation results from number of cross-linker on each SMS-042 devided by the [SH]/[vinyl] value at maximum Young's modulus, i.e. 6/1.2=5.

In our system, the value of f varies from 2 to 5 depending on [-SH]/[vinyl] ratio, therefore M varies from 1800 g/mol to 4500 g/mol assuming number average molecular weight to be 9000 g/mol based on viscosity molecular weight information given by the manufacturer. The phantom equation is applied to our system because of the role of functionality could not be neglected. Combining (eq. 21) and (eq. 23) gives the following equation:

$$G_{ph} = \frac{\rho RT}{Mo} f - \frac{2\rho RT}{Mo} \quad (24)$$

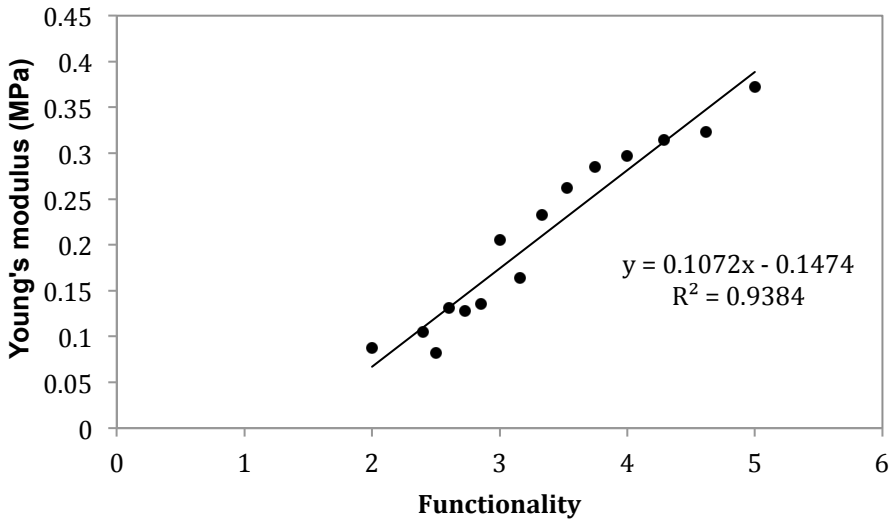

Figure 14. Young's modulus as a function of cross-linker functionality.

Figure 14 showed the linear dependence of Young's modulus to functionality within the range of physically meaningful functionality values.

However, it is not a good fit to the phantom model because the y intercept is not twice of the slope, as suggested by equation 24. This relatively large discrepancy is probably due to the following two reasons. First, the molecular weight of V-PDMS is comparable to that of molecular weight between cross-linkers, therefore should not be ignored when calculating M for equation 21, instead, the combined contribution should be evaluated. Second, the choice of theoretical model could be incorrect. The phantom model and the affine model are two extreme cases in terms of correlating elastic modulus to molecular weight and functionality, so maybe the junction affine model is a better choice for our system. If a good fit model for the experimental data were to be found, then it would provide another method to evaluate the molecular weight of pre-polymer by plotting modulus vs. functionality.

3.1.2 Young's Modulus of PDMS Thin Films Measured by AFM

The homemade tensile test setup provides us with a good estimation of Young's modulus of most of the completely cross-linked PDMS. However, we are also faced with technical difficulties when carrying out the measurement. For example, samples could be too brittle or too fragile to be peeled off from the petri dish; the increment of the weight could be too big for some soft samples so that not enough data were obtained before the sample was broken. Therefore, we started exploring the possibility of adopting AFM nanoindentation as our measurement method. By adopting this novel method,

we can make PDMS thin films supported on silicon wafer, and no longer need to worry about the difficulty of peeling the sample off the supporting material. In addition, AFM nanoindentation allows for measurement of local stiffness at designated locations on the sample, instead of stretching the entire sample for an average stiffness value.

In order to control PDMS substrate stiffness spatially and temporally, we investigated the effects of curing time on Young's modulus and the critical time for the reaction to complete. The optimum ratio of [SH]/[vinyl] = 1.2 was applied to all the reactions that took place in this section. According to Figure 15, Young's modulus of the thin film after 400 s UV irradiation was significantly higher than that after 200 s UV curing, which could be explained by the fact that longer exposure time allowed more radicals to be generated, minimizing the effect of oxygen termination and resulting in a more homogeneous system. Therefore, we hypothesized that photomasking half of the substrate surface area after 200 s UV irradiation while keeping the other half irradiated for another 800 s would create a substrate with significant stiffness difference between the two halves. Unexpectedly, the absolute value for soft and hard domain differed a lot between the curing time experiment (Figure 15) and the photomasking trial (Figure 16). This was likely due to the three-hour delay time in Young's modulus measurement for curing time experiment, whereas the measurement was done immediately after the photomasking trial. However, the sample's sensitivity to time lapse between

fabrication and characterization made us speculate the possible aging process of PDMS substrate and the tip wear out effect on Young's modulus measurement.

The same sample that generated data for Figure 16 was measured again after one week using the same tip to test if aging process existed. A significant increase in Young's modulus has been observed in both the original soft and hard domains as shown in Figure 17. Since this same tip has been used multiple times to obtain force curves on multiple samples, it was speculated that the tip has been worn out and could not give reliable data. However, the results in Figure 18 showed that a new tip generated similar results in both the soft and hard domains of the aged sample, indicating the negligible effects of reusing the tip.

In addition, it was previously expected that after 1000 s UV curing the polymerization would reach completion by incorporating all the pre-polymers into the network. However, as indicated by the data in Figure 19, the extent of reaction depended not only on UV curing time, but also on photoinitiator concentration. Decreasing photoinitiator concentration would decrease initiation rate, thus slowing down the reaction by generating fewer radical chains during a certain period of time. Even though decreasing photoinitiator concentration also has the potential in increasing molar mass of the polymer produced in regular free radical reactions, it is not the case for thiol-ene reaction because of the chain transfer nature of the thiol group. In other words,

all the propagating chain will be prematurely terminated by thiol chain transfer without even attempting to add another vinyl group, thus decreasing photoinitiator concentration would not allow more vinyl groups to be incorporated per propagating chain, instead, it would decrease the number of propagating chains. Within a certain amount of time, fewer cross-links would be formed due to the decreased number of free radicals, thus a decreased extent of reaction.

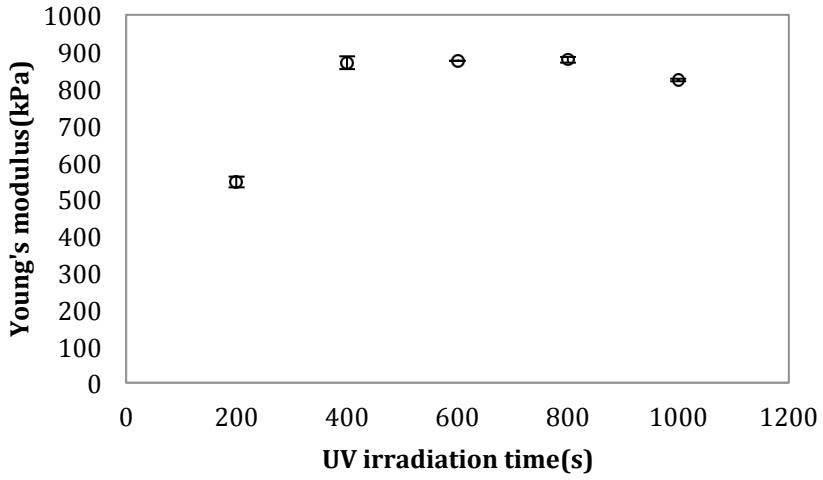

Figure 15. Young's modulus as a function of UV irradiation time. Measurement was carried out 3 h after sample fabrication.

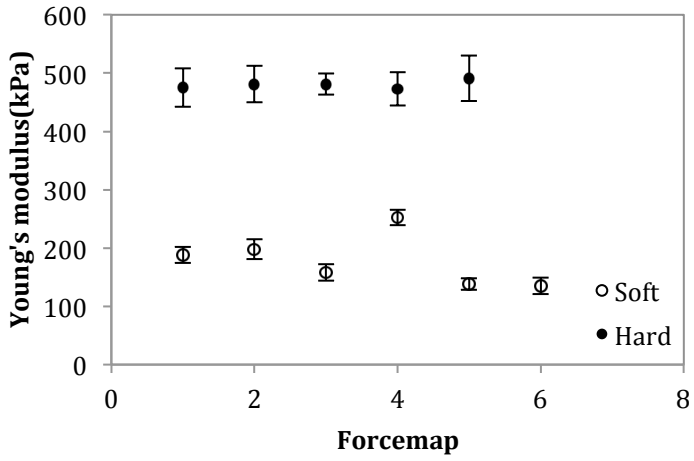

Figure 16. Young's moduli in hard domain resulted from 1000 s UV curing and soft domain resulted from 200 s UV curing.

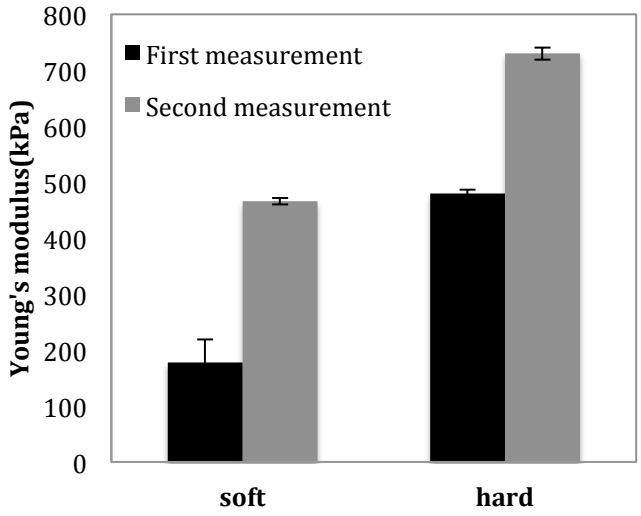

Figure 17. Aging effect on Young's modulus. The same sample was measured twice using the same AFM tip. The first measurement was done immediately after sample fabrication, whereas the second measurement was done one week after the first measurement.

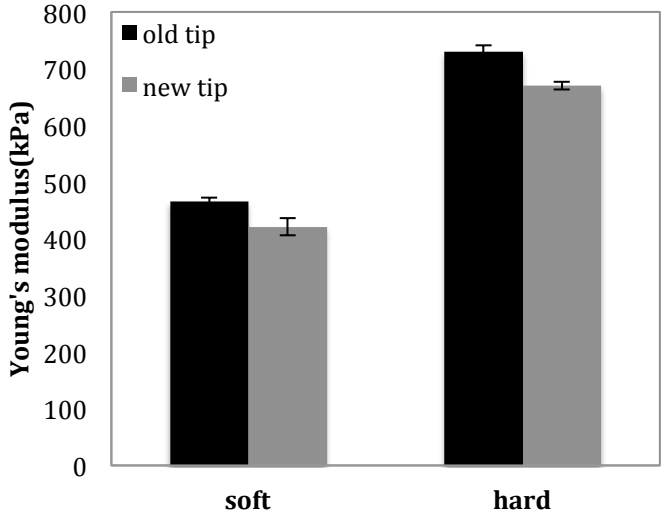

Figure 18. Effects of tip wear out on Young's modulus. Measurement was taken on the same sample using old and new AFM tips one week after sample preparation.

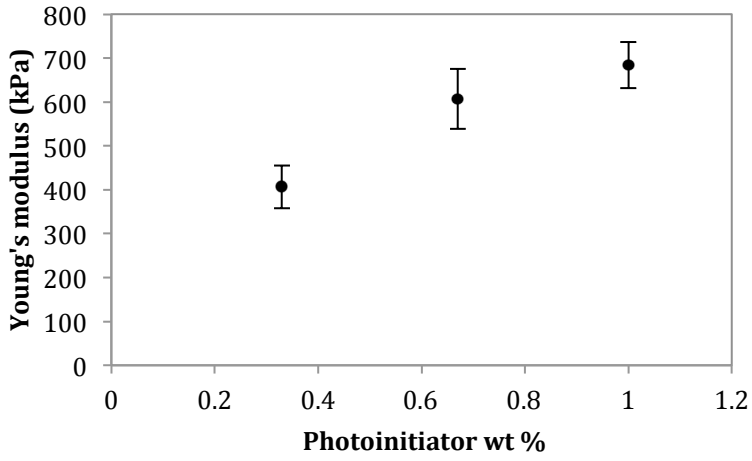

Figure 19. Dependence of Young's moduli on photoinitiator concentration. Samples were measured three hours after sample preparation.

In summary, we varied the molecular weight of the V-PDMS while keeping the SMS042 component constant, and found that the smaller molecular weight PDMS-V05 (800 g/mol) gives the highest Young's

modulus. A follow-up study was carried out to further quantify the effect of functional group ratio on Young's modulus using the V-05 system, and a maximum was found at 1.2 molar ratio between thiol and vinyl groups. The results were then fitted to the phantom model and demonstrated a linear dependence of Young's modulus on cross-linker functionality.

Furthermore, AFM nanoindentation was used to measure Young's modulus of cross-linked PDMS thin film supported on silicon wafer. We found that shorter UV-irradiation time decreased Young's modulus, making it possible to design a substrate containing regions with different stiffnesses by applying a photomask. However, the aging effect caused by incomplete reaction increased Young's modulus post-UV treatment, further complicating the system. Thus, we found that it was more meaningful to look at the AFM results comparatively, i.e. between the control group and experimental group, rather than relying on the absolute value of the results obtained from each trial.

3.2 AFM Parameter Optimization for Nano-indentation Measurement (Thiol-ene System)

Overview In the previous section, we discussed how the aging process of incompletely cross-linked PDMS could affect the Young's modulus measurement. However, it is still very challenging to generate reproducible data using AFM nanoindentation even with completely cross-linked samples due to the different parameters that could be varied during the data acquisition

process. In this section, we varied several important parameters independently to study their effects on AFM nanoindentation measurements in order to generate reproducible results. We mainly focused on the following parameters: film thickness, indenter bead radius, indenting velocity, and trigger force.

According to the Hertz model, in order to simplify Equation 5 to Equation 7, it is assumed that the sample indented can be treated as an infinite half sphere with radius R_2 significantly greater than indenter radius R_1, and R is defined as $R=R_1R_2/(R_1+R_2)$. Therefore, we would expect to find a minimum thickness of the thin film, below which the sample cannot be treated as an infinite half sphere because of the substrate effect.

Recall that

$$\delta = \frac{a_0^2}{R} \tag{5}$$

$$\delta = \frac{a_0^2}{R_1} \tag{7}$$

in which a_0 is the radius of surface of contact, and δ is the depth of indentation.

However, the prerequisite for equation 5 to be valid at the first place is that indentation δ is very small compared to the radius of the indenter. Equation 5 is an approximation of eq. 24 when δ is very small compared to radius of indenter.

$$\frac{a}{\delta} = \frac{R-\delta}{a} \tag{24}$$

Therefore, a comprehensive study of indentation depth δ in relationship to indenter radius R and film thickness d is the main goal of our experiment.

3.2.1 Dependence of indentation depth on film thickness

To obtain thin-film with different thickness, we varied the spin coating rate while keeping the spin coating time constant. The film thickness was measured by profilometer, for which the two boundaries of a silicon-supported thin-film was cut with razor blade, leaving the middle part intact so that the scanning tip moving from one end to the other can generate a profile of the entire film, thus estimating the film thickness. Expectedly, the film thickness decreased as the spin coating rate increased (Figure 20). The data obtained in the range of 700 rpm to 6000 rpm could be fit in the equation y = $10^6 x^{-1.594}$. The exact thickness might vary from system to system due to the viscosity of different pre-polymers used, but the general trend for the dependence of film thickness on spin coating rate should be applicable to other systems as well.

Furthermore, a study of indentation δ in relationship to film thickness d could help define the minimum value of film thickness, above which the slope of indentation vs. trigger force remains constant. This could indirectly define the minimum value of film thickness below which the “infinite half sphere assumption” would no longer be valid. To facilitate the study, the

"twopointE" procedure in Igor has been modified to read indentation δ from the loading curves. Due to hysteresis, loading curve gives a 30-50 nm underestimation of indentation δ, defined as the distance travelled between when force was zero and when force reached trigger force. It still remained a question whether it was necessary and correct to extract indentation from loading curve while extracting Young's modulus from unloading curve.

For all the spin coating rates tested, it has been shown that under the same trigger force, thinner films were indented less compared to thicker films when the same trigger force was applied (Figure 21). Another way of interpreting this figure was that when looking at x vs. y axis, the trigger force vs. indentation plot could still give a sense of Young's modulus. The general trend was that the thinner films had higher Young's modulus compared to the thicker films. The minimum thickness could not be identified because the slopes differed for all four spin coating rates in Figure 22, indicating a strong effect of film thickness on thin-film Young's modulus measurement.

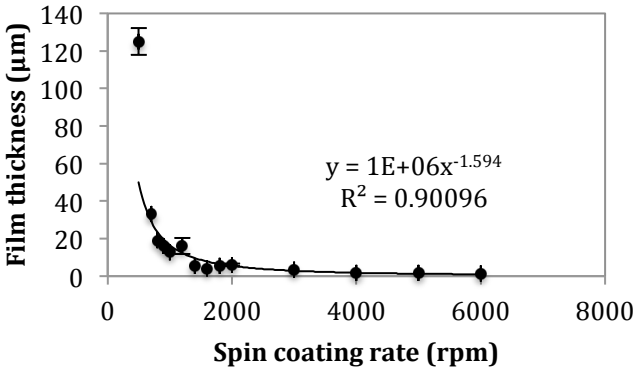

Figure 20. Average film thickness with standard deviation fitted to power equation y = $10^6 x^{-1.594}$. The fit does not include the first point in the plot.

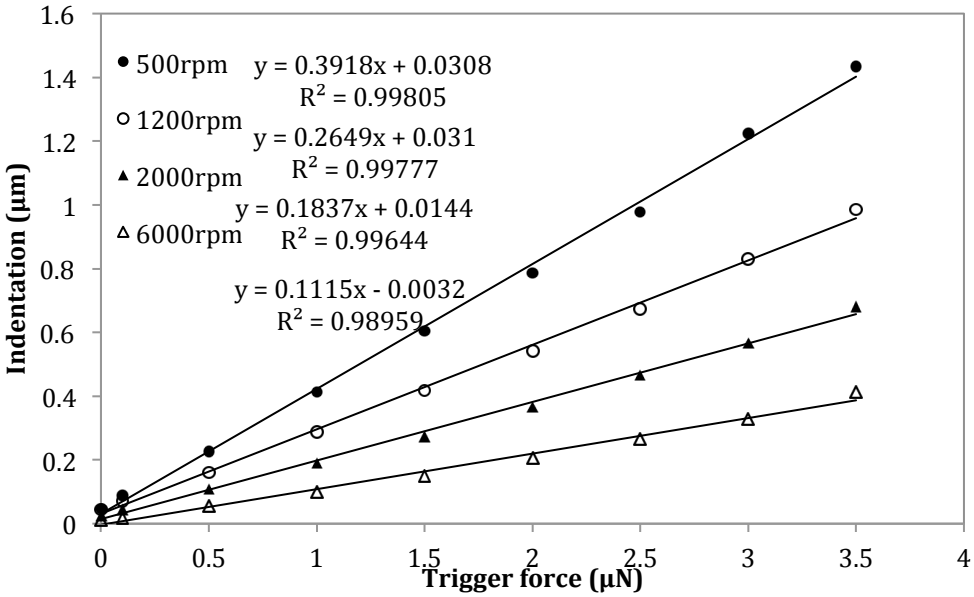

Figure 21. Indentation vs. trigger force for films with different spin coating rate.

3.2.2 Dependence of indentation depth on indenter radius

To vary indenter radius, we tested two beaded-tip with an order of magnitude difference in indenter radius. One has an indenter diameter of 3.5 μm and the other one has a diameter of 45 μm. The velocity was varied within a wide range to explore the viscoelasticity of cross-linked PDMS. Viscoelasticity describes both the viscous and elastic characteristics of materials, which exhibit time-dependent strain. Although the viscoelasticity of PDMS is well-known, many studies in the past have treated PDMS as linear elastic material.[49] Inspired by the study carried out by Pussak et al.,[50] we probed thin film PDMS at different velocity and plotted indentation as well as

Young's modulus against indenting velocity. This approach will not only allow us to identify a velocity range where elastic characteristic dominates, but also depict how Young's modulus could be different at different indenting velocity likely due to viscoelastic property.

Specifically, The results in Figure 22 (a) showed that using 3.5 μm beaded-tip generated smaller Young's modulus measurement than 45 μm beaded-tip. Figure 22 (b) showed that when 3.5 μm beaded-tip was used, the indentation was almost 6 times that of when 45 μm beaded-tip was used. The indentation of 3.5 μm diameter bead into the sample accounts for more than 1/3 of the bead radius, which has very likely violated the assumption that indentation radius is much smaller compared to bead radius. Therefore, even though force curve and Young's modulus could be obtained by the 3.5 μm beaded-tip as well as the 45 μm beaded-tip, we chose to use 45 μm beaded-tip for future study because it obeys the assumption that indentation depth is much smaller compared to the bead radius.

A spin coating rate of 2000 rpm was chosen for future study for two reasons although samples of all thickness assessed showed thickness-dependent Young's modulus values. First, a 2000 rpm spin coating rate resulted a film thickenss of approximately 6 μm, as large as 10 times of the indentation depth for both the 3.5 μm diameter bead and the 45 μm diameter bead. Second, the film thickness generated by 2000 rpm was more reproducible and consistant compared to the lower spin coating rates. Further

studies using 2000 rpm spin coating rate generated Young's modulus measurement of around 450 kPa, comparable to the thick film measurement with minimum effect from trigger force and indentating velocity (Figure 23a). However, the indentation depth generated by 1000 nN trigger force was significantly different compared to the indentation depth generated by 1 nN, 10 nN and 100 nN trigger force (Figure 23b). Since the indentation depth was comparable for 1 nN, 10 nN and 100 nN, only 100 nN and 1000 nN trigger force were compared in future studies to simplify the data acquisition process.

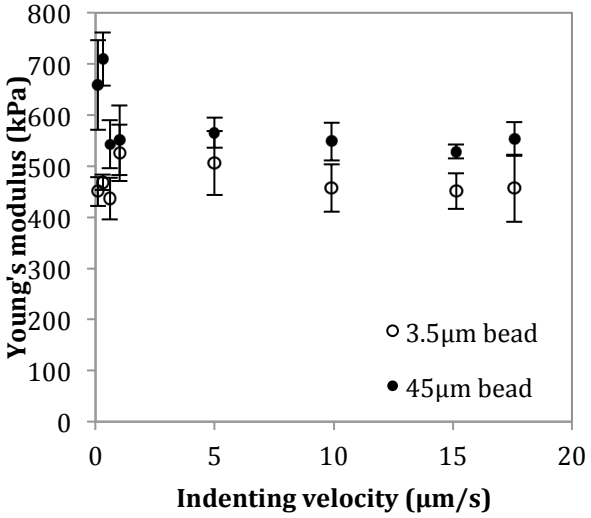

Figure 22 (a). Young's modulus as a function of indenting velocity measured using 3.5 µm beaded-tip and 45 µm beaded-tip.

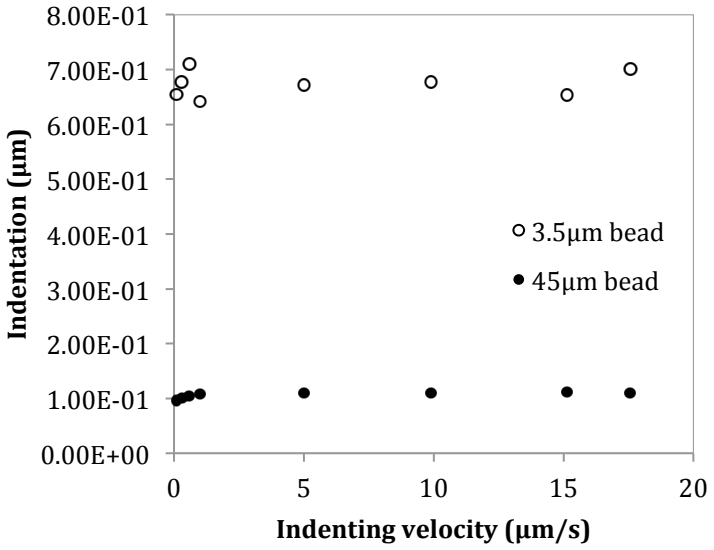

Figure 22 (b). Indentation depth generated at different indenting velocity by 3.5 µm beaded-tip and 45 µm beaded-tip.

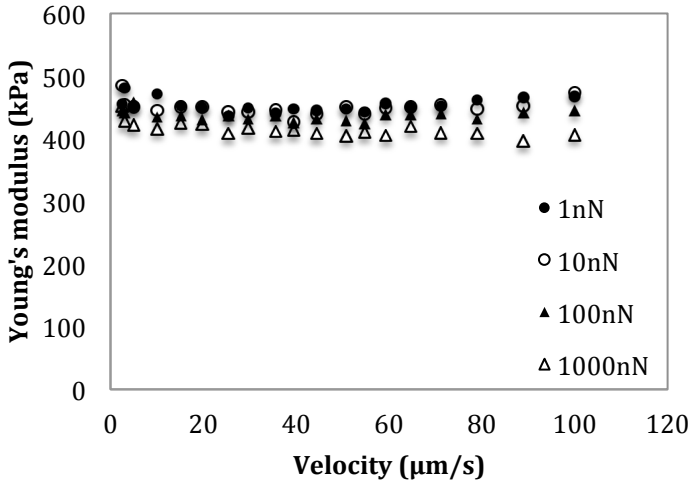

Figure 23 (a). Effect of velocity and trigger force on Young's modulus for V05 thiol-ene system.

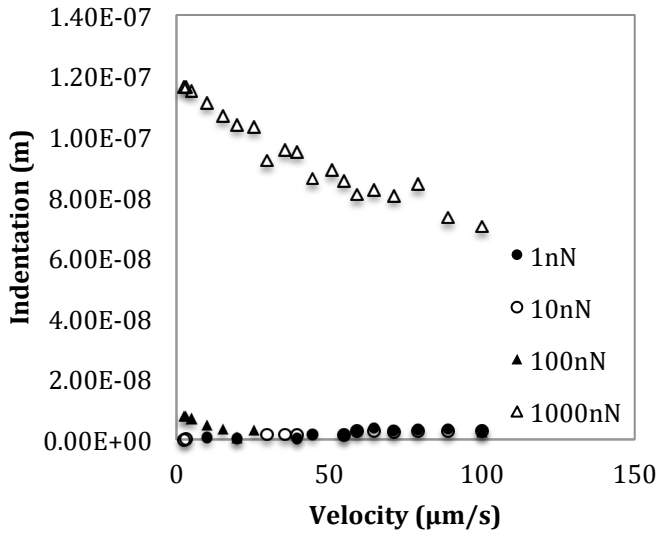

Figure 23 (b). Effect of velocity and trigger force on indentation for V05 thiol-ene system.

In summary, we have identified and studied parameters in AFM nanoindentation that could affect Young's modulus measurement of thin-film PDMS. Film thickness affects surface mechanical property because the thinner the film, the more likely its measured mechanical property is similar to that of its supporting material. Identifying the dependence of Young's modulus on film thickness is the first step in defining the range within which thin film behavior deviates from bulk behavior. In addition, indenter radius and trigger force have been found to affect indentation depth, and a bigger indenter radius is recommended to avoid violating the assumption for JKR model. Although elastic property dominates viscous property for most of the velocity range tested, there were still some deviation when the velocity was extremely low. To ensure reproducibility, experimental parameters including

45 μm diameter beaded-tip, 14 μm/s indenting velocity, 2000 rpm spin coating rate have been consistently applied to all future experiments.

3.3 Effects of Collagen Adsorption and Plasma Oxidation on Surface Chemical and Mechanical Property of PDMS (Hydrosilylation System)

Overview After studying thiol-ene system and optimizing the AFM nanoindentation parameters in the previous studies, our final goal was to answer the intriguing questions: how does surface modification strategies such as plasma oxidation and collagen adsorption affect surface mechanical property? Our original plan was to fabricate four types of surfaces: native PDMS, plasma oxidized PDMS, and collagen coating on both types of PDMS surfaces. However, we encountered the difficulty that thiol-ene cross-linked PDMS undergoes rapid hydrophobic recovery and that the extent of hydrophilization was not reproducible (Table 2). We therefore revisited the hydrosilylation reaction, which is different from the thiol-ene reaction in that Si-H group is the functional unit instead of the S-H group in the cross-linker. Using the hydrosilylation system, we were able to obtain hydrophilized surface via plasma oxidation in a reproducible manner, and maintain the surfaces at low contact angles for at least one week. Fortunately, our efforts in optimizing parameters involved in AFM nanoindentation could still provide us guidance in making reproducible measurement for the cross-linked hydrosilylation system. We were able to fabricate the four different surfaces

mentioned above using the hydrosilylation system, and characterize the surface chemical and mechanical properties using contact angle goniometry, AFM topography scan, AFM nanoindentation, and X-ray photoelectron spectroscopy.

Table 2. V-05 thiol-ene system hydrophobic recovery after 2 min plasma activation.

Time from plasma treatment (h)	Contact angle (°)	
	Advancing	Receding
0.25	38	29
0.5	55	48
1	61	51
6	74	64
19	78	68
90	83	69
168	86	73
285	86	76
522	94	79
Control	104	77

3.3.1 Redefining Parameters for the New System

In order to study the effects of surface modification on surface mechanical properties, it is important to minimize the thickness-dependence of the Young's modulus measurement. However, in the presence of Karsted's catalyst, vinyl terminated PDMS and hydromethylsiloxane could cross-link very quickly even before spin coating, making it necessary to add toluene to the mixture to slow down the reaction. To pick a toluene concentration that would delay cross-linking while minimizing the effect of film thickness on

Young's modulus measurement, we measured Young's modulus of cross-linked PDMS resulting from different toluene concentrations at different indenting velocity. The results in Figure 24 suggested that adding 20% toluene to the pre-polymer mixture helped to slow down the cross-linking while keeping the Young's modulus close to the 0% toluene sample, whereas the 33% toluene sample had a significant increase in Young's modulus measurement likely due to the substrate effect.

PDMS substrates were treated under plasma oxidation for different amounts of time and monitored for 20 h after plasma oxidation to assess hydrophobic recovery rate. A typical native PDMS sample has a dynamic contact angle of 112°/104°. Oxygen plasma treatment generates oxygen species such as O_2^+, O_2^-, O_3, O, O^+, O^-, which can react with the methyl groups on PDMS to hydrophilize the surface. To ensure that there is a significant change in contact angle after plasma oxidation and that the change can last for a relatively long period of time, plasma oxidation time of 15 s, 30 s, 60 s, and 120 s were tested. The trends in Figure 25ab showed that 60 s was the most desirable treatment time because it resulted in a significant drop of advancing and receding contact angles compared to 30 s treatment, while 120 s treatment did not generate further drop in receding contact angle compared to 60 s treatment. Therefore, 60 s plasma oxidation was set as the standard treatment time for this experiment and a longer hydrophobic recovery study was carried out for this condition. Figure 26 suggested that 60 s plasma

oxidation resulted in a hydrophilic surface (~35°/18°) after 1 week of plasma treatment.

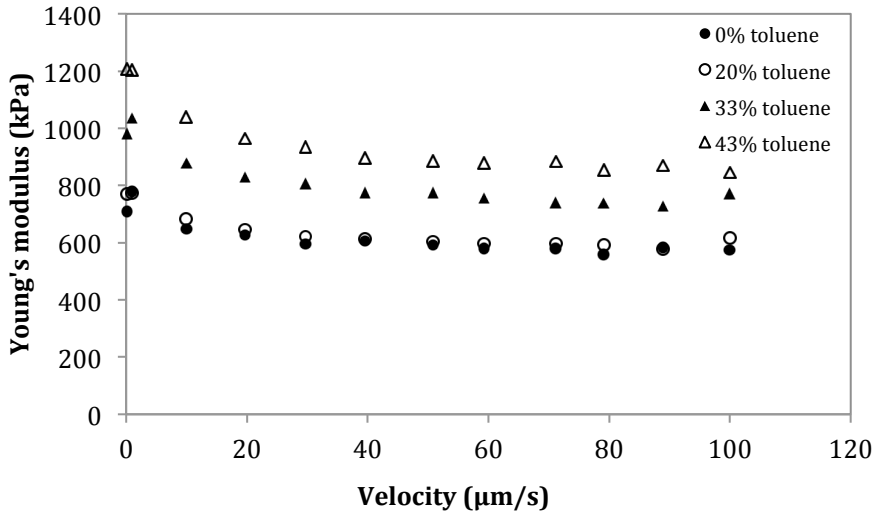

Figure 24. Young's modulus of samples with different toluene dilution at different indentation velocities using 1000 nN trigger force.

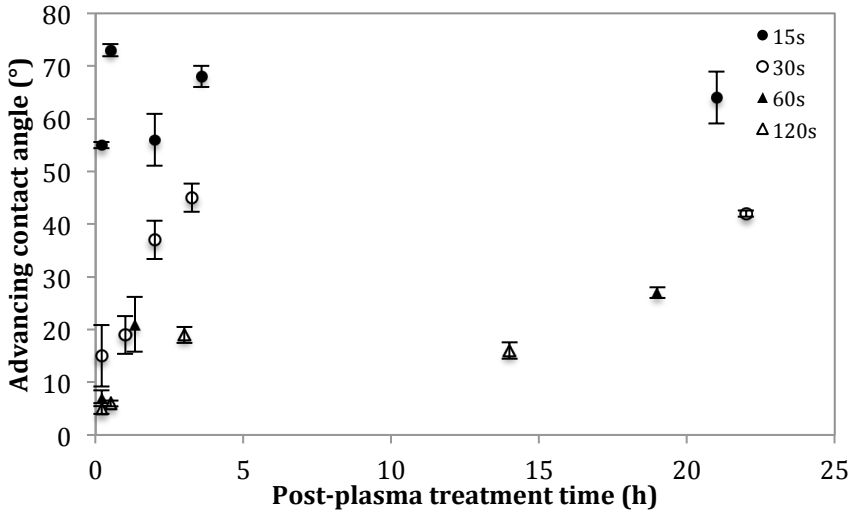

Figure 25 (a) Advancing contact angle of plasma-oxidized PDMS with various plasma-oxidation time monitored for 24 h post-treatment.

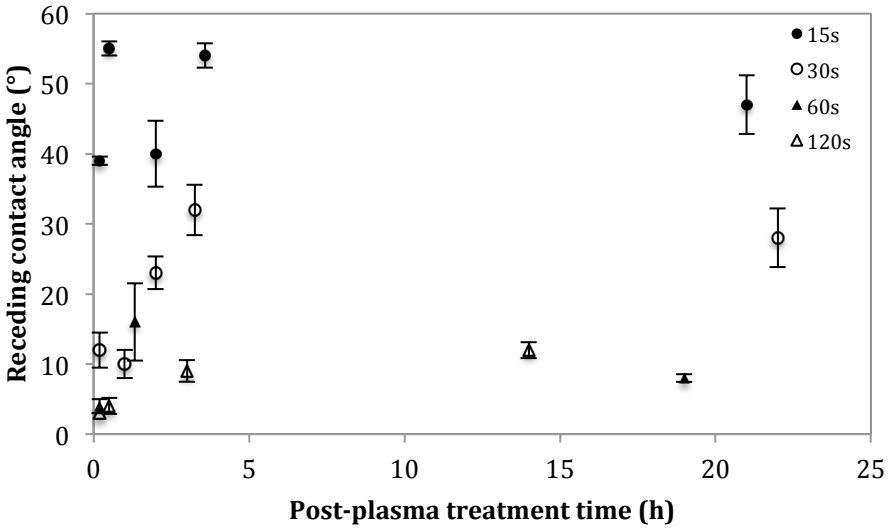

Figure 25 (b) Receding contact angle of plasma-oxidized PDMS with various plasma-oxidation time monitored for 24 h post-treatment.

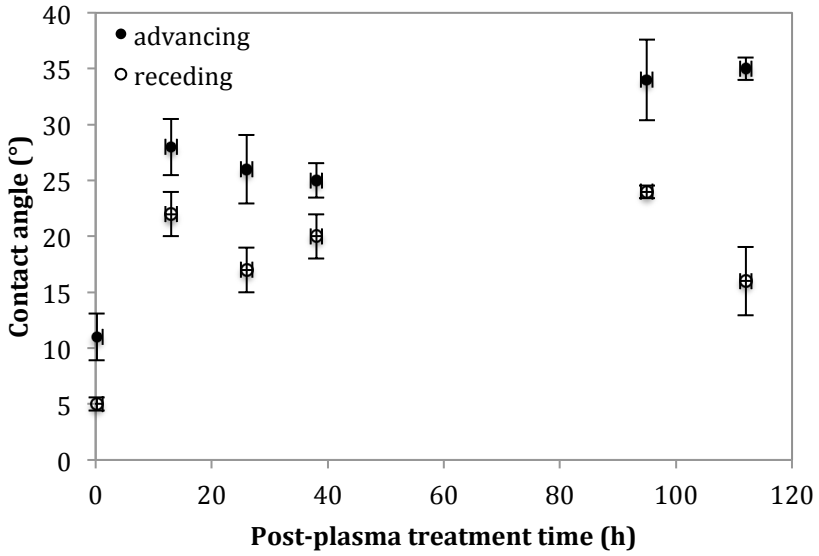

Figure 26. Dynamic contact angle of 60 s-plasma-oxidized PDMS monitored over 120 h.

3.3.2 Surface Characterization Using Contact Angle Goniometry, AFM and XPS

Dynamic Contact Angle: Surface hydrophilicity changed dramatically after plasma oxidation and collagen adsorption. According to Figure 27, native PDMS had a contact angle of 112°/104°, the most hydrophobic and chemically homogeneous surface among these four types of surfaces. Plasma oxidized PDMS had a contact angle of 25°/20° (20 h after treatment), the most hydrophilic and chemically homogeneous surface. Collagen adsorption made the surface more heterogeneous: collagen on native PDMS dramatically decreased the receding contact angle, while collagen on oxidized PDMS significantly increased the advancing contact angle. The results suggested that collagen coating on native PDMS increased its surface hydrophilicity. This is likely because the hydrophobic domain of collagen interacts with hydrophobic PDMS surface, exposing the hydrophilic domain to air and thus decreasing its receding contact angle. The results also suggested that collagen coating on oxidized PDMS increased its surface hydrophobicity. This is likely because the hydrophilic domain of collagen interacts with hydrophilic oxidized PDMS surface, exposing the hydrophobic domain to air and thus increasing the advancing contact angle. Since 24 h collagen adsorption gave a more significant drop on receding contact angle of native PDMS and a more significant increase on advancing contact angle of oxidized PDMS, it suggested that 24 h adsorption could facilitate a better protein coverage.

To assess the data reproducibility, a repeat of the first experiment was carried out, but only using 24 h collagen adsorption. As shown in Figure 28, the contact angle results of collagen on native PDMS for 24 h in the second trail matched that of collagen on native PDMS for 1 h in the first trial. This suggested that although the general trend was reproducible, the absolute value might be slightly different from trial to trial. In addition, 24 h adsorption might generate the same protein coverage compared to 1 h adsorption, as suggested by the adsorption kinetics study of collagen, fibronectin, BSA. The study showed that adsorption reaches plateau after 60 min for fibronectin and BSA, and after 150 min for collagen.[43]

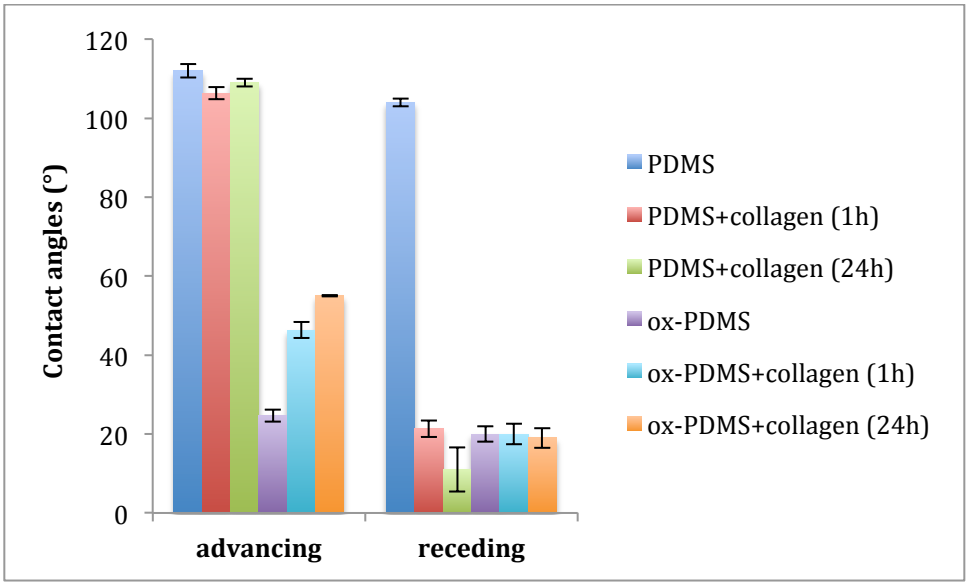

Figure 27. Dynamic contact angle of the four different surfaces, in addition to 1 h collagen adsorption on native and oxidized PDMS.

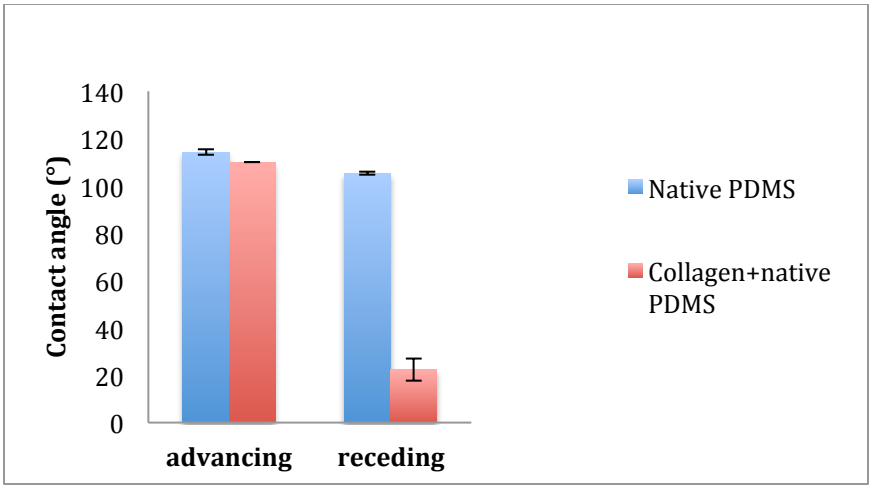

Figure 28. Dynamic contact angle of native PDMS and collagen on native PDMS after 24 h adsorption.

AFM topography scan: The first set of experiment includes topography scans (20 μm× 20 μm) for four different surfaces: native PDMS, collagen coated native PDMS, oxidized PDMS, and collagen coated oxidized PDMS. All samples were imaged after overnight drying in a desiccator. A representative scan was shown in Figure 29 below. Interestingly, irregular honeycomb features were observed on collagen coated native PDMS, but not on any other surfaces.

	Native PDMS	Oxidized PDMS
No collagen	RMS roughness: 1.36 nm	RMS roughness: 1.57 nm
	a.	b.
	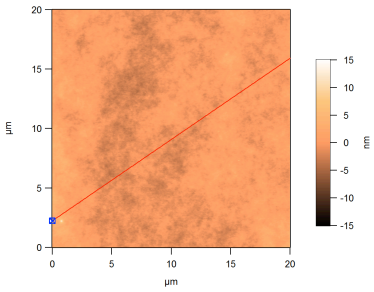	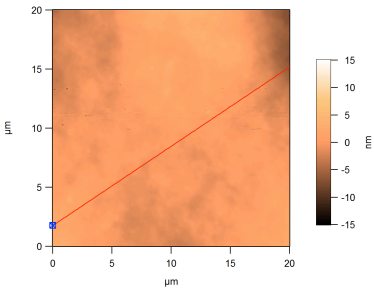
Collagen	RMS roughness: 18.0 nm	RMS roughness: 1.42 nm
	c.	d.
	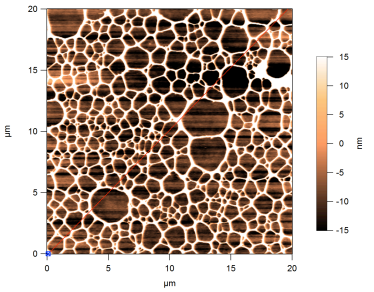	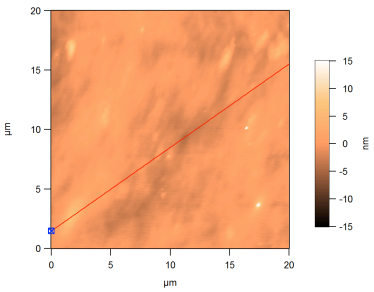

Figure 29. AFM topography scans of native PDMS (a), oxidized PDMS (b), collagen on native PDMS (c) and collagen on oxidized PDMS (d). The red line was drawn on the screen to obtain further information on height profile of the sample across a specific line, and it was not part of the topography image.

In the second set of experiment, when collagen on oxidized PDMS was further evaluated, certain features were found on the surface that led to an increase in RMS roughness. To further investigate the nature of these features, oxidized PDMS samples were soaked in PBS+collagen or PBS alone. Even though aggregates were found more frequently on oxidized PDMS soaked in collagen+PBS, similar features were also found on oxidized PDMS soaked in

PBS alone. Note the height images in Figure 30 for the zoomed in features were very similar for the sample in PBS+collagen and the sample in PBS alone. Thus, these aggregates were more likely to come from PBS than collagen solution.

	20 µm × 20 µm scan	Zoomed in scan (Height)
In PBS + Collagen	RMS roughness: 14.6 nm a.	b.
In PBS	RMS roughness: 11.4 nm c.	d.

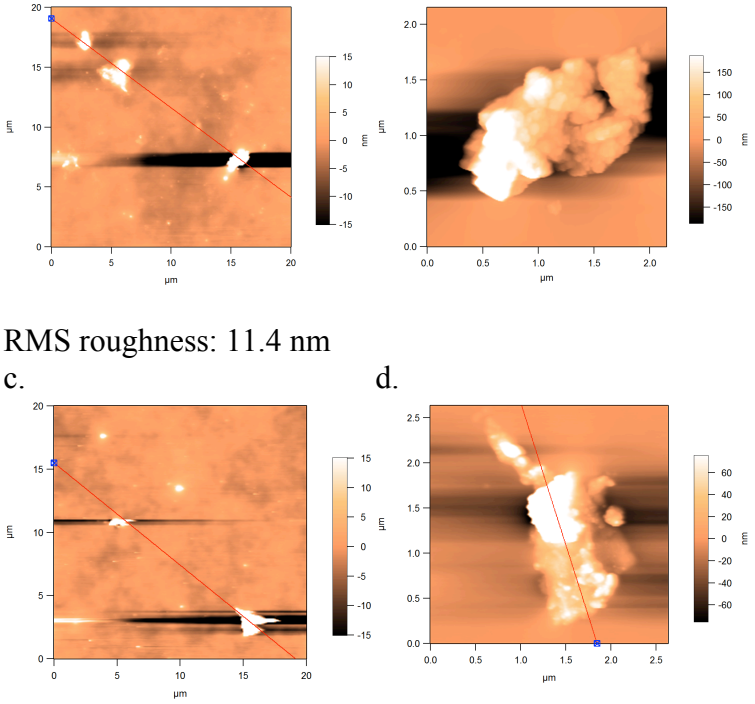

Figure 30. AFM topography scans of overnight-dried oxidized PDMS in PBS+collagen (a.b) and oxidized PDMS in PBS (c.d) The white feature on the middle-right of (a) was zoomed in to generate (b); the white feature on the lower-right corner of (c) was zoomed in to generate (d).

The third set of experiment evaluated topography of collagen on native PDMS. Three (20 µm× 20 µm) random spots were scanned on the collagen+

native PDMS surface. Figure 31 showed that height trace and retrace, phase trace and retrace for the same spot were all consistent with each other, confirming that the features were real. Note that the sizes of honeycombs appeared to be different at different spots. It would be exciting to further investigate the de-wetting process that lead to the formation of these honeycomb structures.

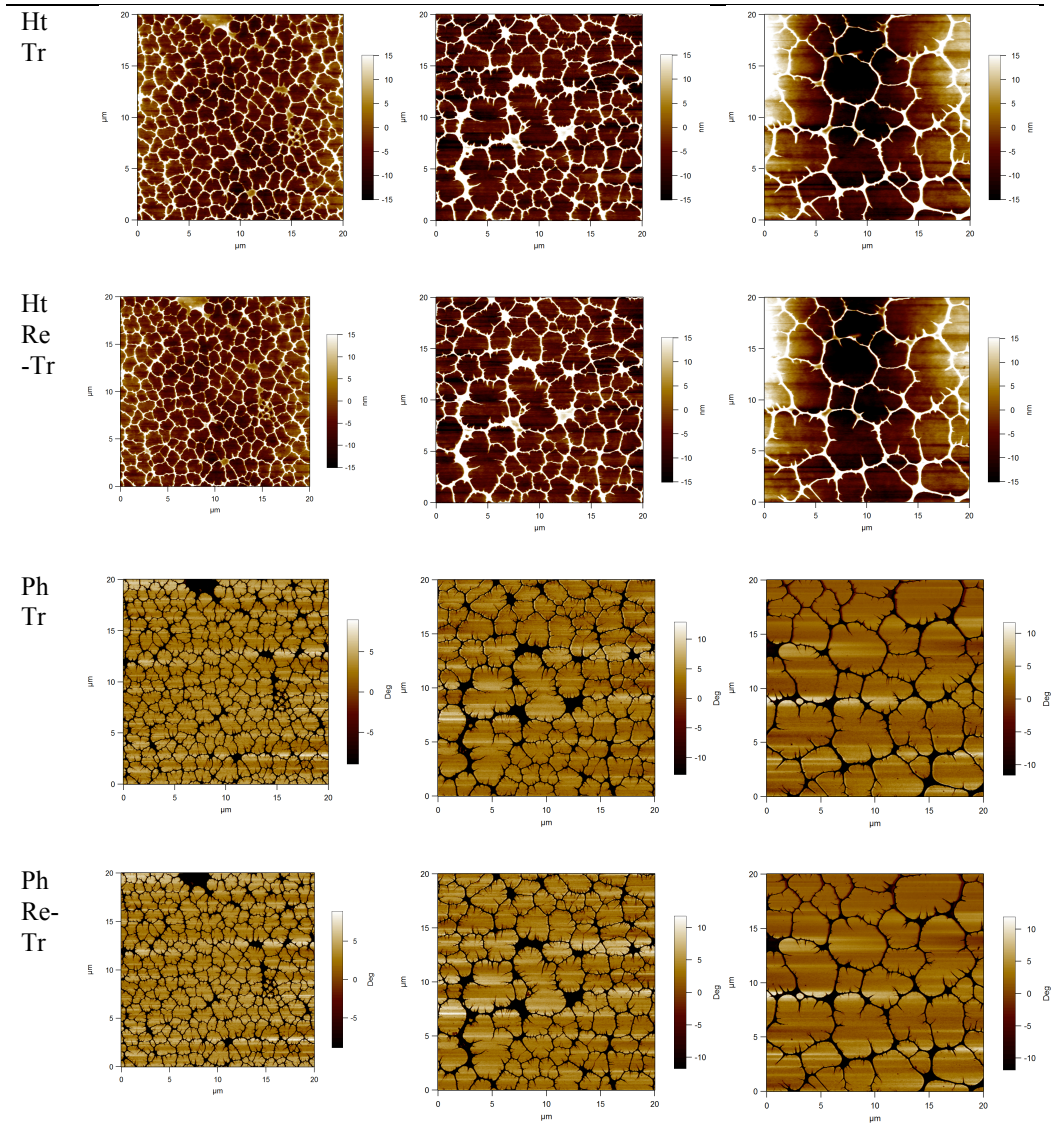

Figure 31. AFM topography scans of collagen on native PDMS at three randomly selected spots. Height trace (first row), height retrace (second row), phase trace (third row), and phase retrace (fourth row) were all consistent with each other for a given spot.

AFM Nanoindentation: Force curve analysis can provide important information about surface mechanical properties. A typical force curve was shown in Figure 9. In this study, we extract Young's modulus (the linear portion of stress/strain) (Figure 32a), pull-off force (the maximum force required to separate tip and sample) (Figure 32b), indentation depth (the distance that bead moves into the sample) (Figure 32c), and Wpull (the area between x axis and blue retraction curve) (Figure 32d) from the force curve using automated Igor procedure. Comparing native PDMS and oxidized PDMS, native PDMS requires a greater pull-off force, has a higher Young's modulus, greater Wpull, and smaller indentation depth (Figure 32). These results suggested that plasma oxidation significantly decreased the adhesion energy between surface and tip, likely because the hydrophilization of PDMS surface has changed the interaction between tip and sample from hydrophobic (polystyrene bead)-hydrophobic (PDMS surface) to hydrophobic (polystyrene bead)-hydrophilic (oxidized PDMS). To confirm the hypothesis, it would be informative to use COOH modified tip to approach the surface. A reasonable prediction would be that there would be a greater adhesion between COOH modified tip and oxidized PDMS compared to native PDMS.

It has been found in that collagen coated native PDMS have a slightly higher average Young's modulus than native PDMS alone, likely due to the effect of the adsorbed collagen. Results also showed that the 1000 nN trigger force curves having a higher average modulus compared to that of the 100 nN trigger force for collagen coated surfaces, but not for native or oxidized PDMS surfaces. Approximately, when 100 nN trigger force was applied, the indentation area was a 1.3 μm diameter circular footprint; when 1000 nN trigger force was applied, the indentation area was a 4.2 μm diameter circular footprint. A greater indentation area indicated a higher chance of landing on a collagen fiber, thus a higher average modulus. In terms of oxidized PDMS and collagen on oxidized PDMS, further experiments using XPS is needed to detect the composition of the aggregates found on these surfaces.

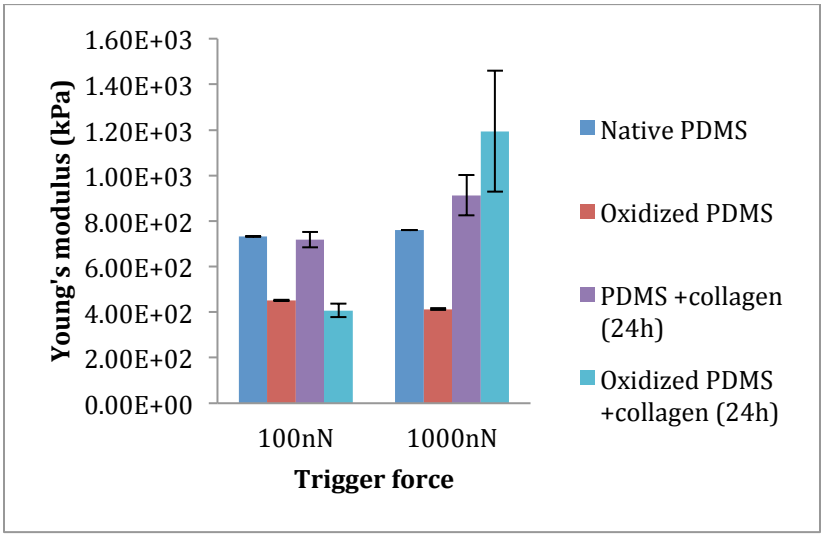

Figure 32 (a). Plots of average values and their standard deviation for Young's modulus for four surfaces of interest.

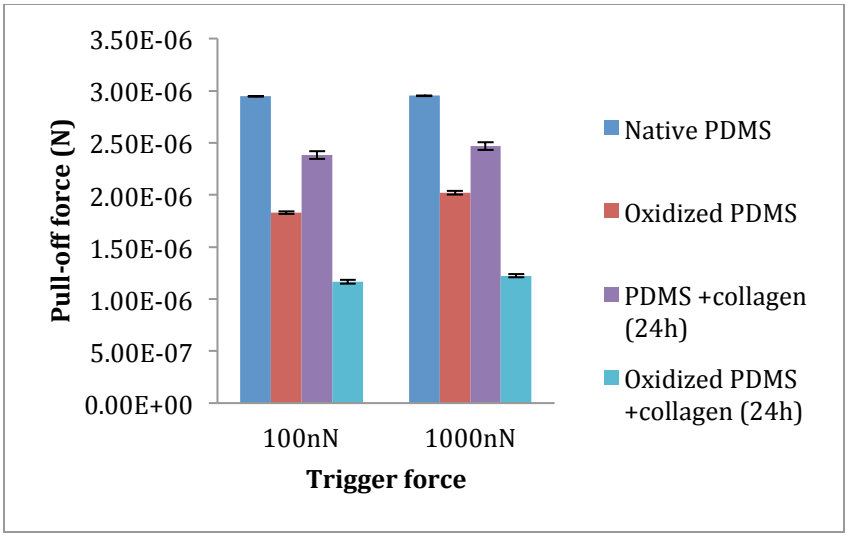

Figure 32 (b). Plots of average values and their standard deviation for Pull-off force for four surfaces of interest.

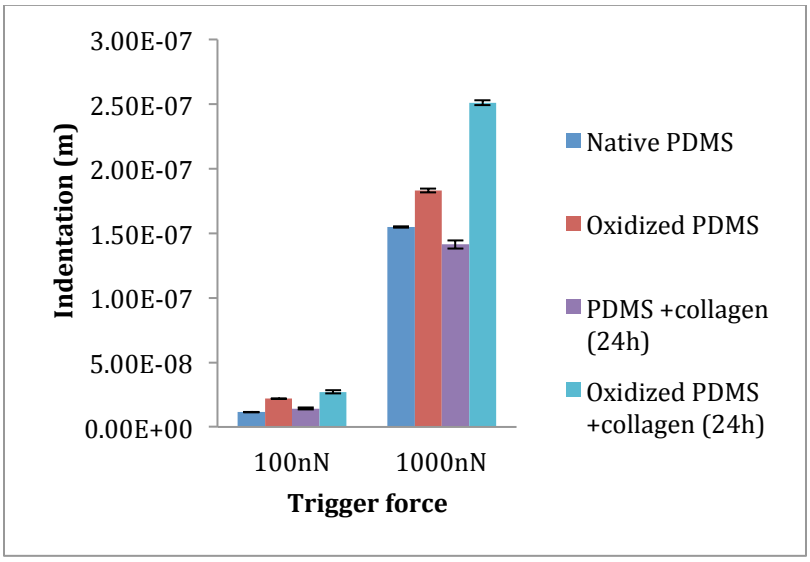

Figure 32 (c). Plots of average values and their standard deviation for indentation depth for four surfaces of interest.

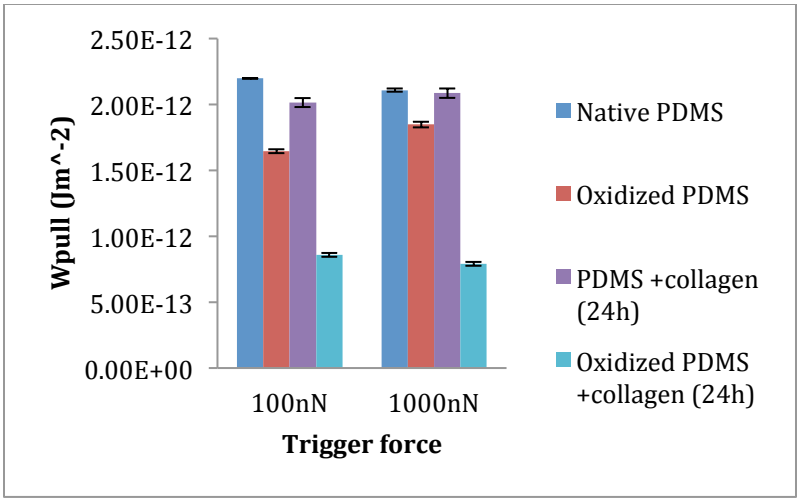

Figure 32 (d). Plots of average values and their standard deviation for adhesion energy for four surfaces of interest.

XPS results: Initially, an XPS survey was carried out on all four surfaces of interest, with two duplicates for each surface type (Table 3). The results showed a significant increase in oxygen composition on the oxidized PDMS compared to the native PDMS. In addition, nitrogen composition was greater for collagen-coated surfaces compared to surfaces with no collagen coating, although the large standard deviation was concerning due to small sample size. A closer look at the native PDMS using XPS multiplex resulted in an atomic composition ratio very close to the ratio of carbon, silicon, and oxygen in PDMS pre-polymers (2:1:1), confirming the purity of the material used in the experiment and the validity of XPS measurement (Table 4). Overall, XPS results gave a clear indication of the difference in atomic composition across all four surfaces of interest.

Table 3. Atomic composition of C1s, O1s, Si2s, and N1s for four surfaces of interest obtained via XPS survey (2 sample spots per data point). *Note: the large standard deviation was due to small sample size.

	C1s	O1s	Si2s	N1s
Native PDMS	45.1±1.6	31.4±0.4	23.6±1.3	<0.1
Ox-PDMS	21.0±8.3	55.3±8.3	23.1±0.2	<0.1
Col-nat-PDMS-24h	44.7±2.6	32.4±1.1	22.3±0.6	0.7±1.0*
Col-ox-PDMS-24h	41±4.7	34.7±6.6	22±5.1	2.25±3.2*

Table 4. Atomic composition of C1s, O1s, Si2s, and N1s for collagen coated native PDMS and its control surfaces obtained via high resolution XPS multiplex (4 sample spots per data point).

	C1s	O1s	Si2s	N1s
Native PDMS	49.9±0.7	26.6±0.1	23.3±0.5	<0.1
Native PDMS in PBS (24h)	49.4±0.9	26.8±0.3	23.7±1.3	0.1
Native PDMS in collagen (24h)	48.9±0.6	27.3±0.2	23.0±0.7	0.8±0.3
Native PDMS in collagen (1h)	48.5±0.6	27.4±0.4	23.7±1.0	0.4±0.1

3.3.3 Using 3D Forcemap Image to Study Heterogeneous Surface Topography

For proof of concept study to figure out whether extremely high modulus corresponds to collagen fiber adsorption on native PDMS, high-resolution force maps were taken to visualize the topography of the surface and to assess the stiffness at each individual point. The HtF image extracts contact points at each location; in other words, it records the place where the software labeled as “0” on the force curve. This HtF image indirectly gives the

topography image if taken at high-enough resolution. For example, the HtF image shown in Figure 33 clearly showed some high features that might be collagen fibers at discrete locations. Now the question remains: why do we only get a few "high" modulus measurements while having such good collagen coverage?

We hypothesized that most indentation happened at the empty space (Figure 34a). Sometimes the bead hit the fiber but fall over, and that was why some of the force curves had a fluctuation on the extension curve (Figure 34b). In the rare cases when bead hit right on the fiber (Figure 34c), the modulus is extremely high. The measurement of Young's modulus at these locations were in the same range as the stiffness results of the single fibril measured by Yang *et al.*[49] Note how different the pull-off force was between hitting the fiber and hitting the PDMS background. There was basically no adhesion between the fiber and the bead.

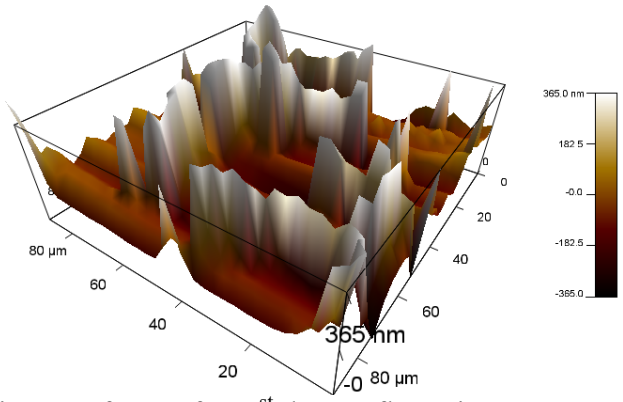

Figure 33. 3D image of HtF after 1st degree flattening. 100 nN trigger force, 14 µm/s indenting velocity, and 45 µm diameter beaded-tip were used for this experiment. The force map were taken at a 90 µm *90 µm area with 32 points *32 lines spacing.

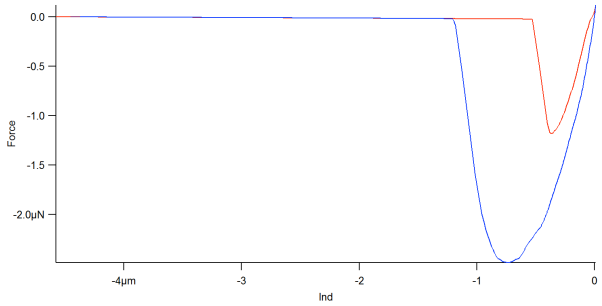

Figure 34 (a). Force curve of a beaded-tip hitting a blank spot, i.e. the PDMS substrate.

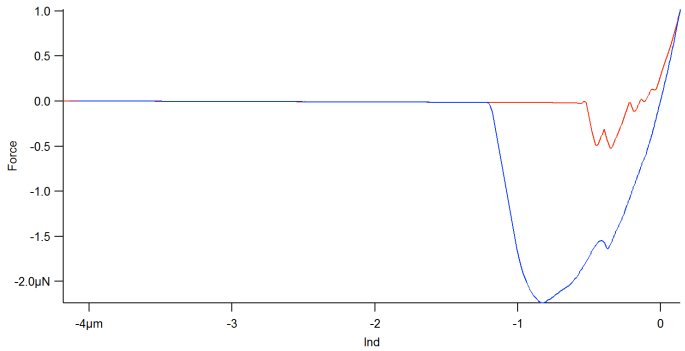

Figure 34 (b). Force curve of a beaded-tip hits a fiber and then falls off.

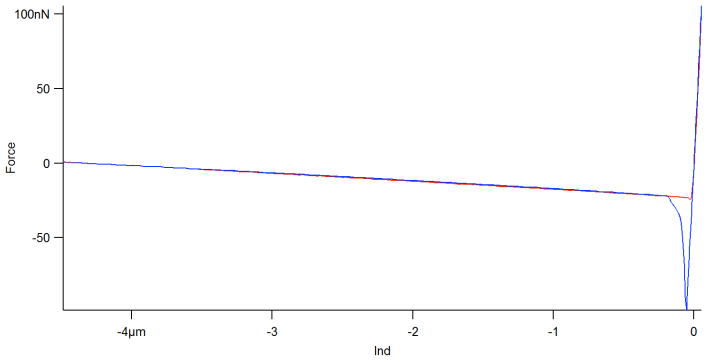

Figure 34 (c). Force curve of a beaded-tip hitting directly on a fiber.

In summary, plasma oxidation and collagen adsorption on cross-linked PDMS have an impact on its surface chemical and mechanical properties. It is interesting to observe the difference in topography between collagen coated

native PDMS and collagen coated oxidized PDMS, noting that both types of surface have the ability to have collagen deposition. Furthermore, our results showed that oxidized PDMS has lower Young's modulus than native PDMS, likely due to the change in chemical property at the top layer of the sample. In addition, collagen coated PDMS has higher Young's modulus than non-coated PDMS, likely due to the dehydrated collagen on top of the surface layer of cross-linked PDMS. Lastly, we suggest the HtF image of the 3-D forcemap as a possible new way of visualizing the topography of the sample corresponding the force curves to the features in 3-D map.

CHAPTER 4. CONCLUSIONS AND FUTURE DIRECTIONS

PDMS is an important polymer with a wide range of applications in food industry, cosmetics, and biomedical field. Understanding its mechanical property is especially crucial for mechanobiology research, which motivated the special focus of this research direction on the effect of mechanical cue on cell behavior. Through this collaborative study in materials chemistry and physics, we achieved a better understanding of the mechanical property of PDMS from different aspects including fabrication, characterization, and surface modification.

Fabrication. Thiol-ene chemistry was applied in the photo-polymerization reaction to create a homogeneous system with high conversion rate. Parameters such as pre-polymer molecular weight, functional group ratio, UV irradiation time and photoinitiator concentration were varied to assess their effects on the extent of cross-linking as characterized by Young's modulus. The results from tensile test suggested that cross-linking density increased as molecular weight of vinyl-terminated PMDS decreased, and that there was a linear dependence of Young's modulus on cross-linker functionality within the range of $2 \leq f \leq 5$. In addition, results from AFM nanoindentation demonstrated that it was possible to create a mechanically heterogeneous surface with different Young's moduli in different regions by imposing photo-mask to allow varied UV-irradiation time, although sample

aging need to be considered using this method. Furthermore, photoinitiator concentration affected the rate at which radicals were generated, with a higher photoinitiator concentration resulting in a higher cross-linking density. For future studies, we would like to utilize photolithography to fabricate microfluidic device with controlled modulus for application in mechanobiology research.

Characterization. Besides using the commonly adopted tensile test and obtaining comparable results from the homemade tensile tester and the Instron instrument, we studied and optimized the AFM nanoindentation method that is particularly suited for measurement of heterogeneous, soft biomaterials such as PDMS and hydrogels. The assumptions for JKR model were revisited and the relationships among three major parameters were studied: the indenter radius R, the film thickness d, and the indentation depth δ. In order for the indentation depth to be very small compared to the indenter radius, the AFM tip with a bead diameter of 45 μm was chosen to replace the previously used beaded-tip of 3.5 μm in diameter. The thin film thickness was plotted against spin coating rate, and their relationship was described by a polynomial fit. Lastly, the indentation depth could be varied by both the magnitude of trigger force and the bead diameter, with the smaller bead and higher trigger force generating the greater indentation depth. The preliminary study on the above mentioned factors revealed that experimental data can be reproducibly obtained when the following set of parameters are used: AFM tip

radius is 22.5 μm, tip spring constant is 7.5 N/m, indentation velocity is 14 μm/s, trigger force is 1000 nN, and spin coating rate is 2000 rpm. One remaining problem need to be solved: very often the sample surface is not completely cross-linked due to oxygen interference, so it remains a challenge for tip to pull-off from the surface when the surface is sticky. We are proposing two solutions that need to be further tested: the first method is to use tip with greater spring constant, so that the tip could be pulled off before reaching the deflection limit; the second method is to carry out the measurement in detergent, which has been shown to require minimal pull-off force and work of adhesion.

Surface modification. In the last phase of this study, we investigated the effects of collagen adsorption and plasma oxidation on surface chemical and mechanical properties of PDMS. Collagen coating is of significant biological relevance because it is widely used in *in vitro* studies of single cell dynamics to achieve better cell adhesion. The preliminary results suggested that collagen fiber formed uniform honeycomb structures on native PDMS, but not on oxidized PDMS. In addition, collagen adsorption on native PDMS led to an increased average Young's modulus compared to native PDMS, suggesting that dehydrated collagen fiber has a higher stiffness compared to PDMS substrate. Moreover, it has been consistently observed that plasma oxidation resulted in a decreased adhesion between polystyrene bead and PDMS surface, as well as a decreased Young's modulus of the substrate.

Change of surface chemical and mechanical properties of PDMS after collagen adsorption is likely to contribute to the better understanding of single cell dynamics on surfaces with tunable chemical and mechanical properties. For future directions, we would like to carry out surface topography scan and nanoindentation in PBS to better mimic the real conditions in biological research, and to explore whether changing the hydration status of collagen will change its chemical and mechanical properties.

REFERENCES

[1] Martin, P. Wound healing: aiming for perfect skin regeneration. *Science* **1997**, 276, 75-81

[2] Springer TA. Traffic signals for lymphocyte recirculation and leukocyte emigration: the multistep paradigm. *Cell* **1994**, 76, 301–314.

[3] Bernstein, L. R., and Liotta, L.A. Molecular mediators of interactions with extracellular matrix components in metastasis and angiogenesis. *Curr. Opin. Oncol*. **1994**, 6, 106 –113.

[4] Boyden S. The chemotaxtic effect of mixtures of antibody and antigen on polymorphonuclear leucocytes. *J. Exp. Med.* **1962**, 115, 453– 466.

[5] Stossel T.P. On the crawling of animal cells. *Science.* **1993**, 260, 1086–1094.

[6] Carter SB. Haptotaxis and the mechanism of cell motility. *Nature.* **1967**, 213, 256 –260.

[7] Lowe, B. The role of Ca2_ in deflection-induced excitation of motile, mechanoresponsive balancer cilia in the ctenophore statocyst. *J. Exp. Biol*. **1997**, 200, 1593–1606.

[8] Erickson, C. A., and Nuccitelli, R. Embryonic fibroblast motility and orientation can be influenced by physiological electric fields. *J. Cell Biol*. **1984**, 98, 296 –307

[9] Saranak, J., and Foster, K.W. Rhodopsin guides fungal phototaxis. *Nature.* **1997**, 387:465–466.

[10] Lo, C.M., Wang, H.B., Dembo, M., and Wang, Y.L. Cell movement is guided by the rigidity of the substrate. *Biophys J.* **2000**, 79, 144-152

[11] Alberts, B. Essential Cell Biology, third edition. New York: Garland Science, **2010**. Print.

[12] Wang, N., J. P. Butler, and Ingber, D.E. Mechanotransduction across the cell surface and through the cytoskeleton. *Science.* **1993,** 260,1124–1127.

[13] Choquet, D., Felsenfeld, D.P. and Sheetz, M.P. Extracellular matrix rigidity causes strengthening of integrin-cytoskeleton linkages. *Cell* **1997**, 88, 39–48.

[14] McDaniel, D.P., Shaw, G.A., Elliott, J.T., Bhadriraju, K., Meuse, C., Chung, K-H., Plant, A.L. The stiffness of collagen fibrils influences vascular smooth muscle cell phenotype. *Biophys. J*. **2007**, 92, 1759-1769.

[15] Engler, A.J., Sen, S., Sweeney, H.L., Discher, D.E. Matrix elasticity directs stem cell lineage specification. *Cell*. **2006**, 126, 677-689.

[16] Zhang, W.J., Choi, D.S., Nguyen, Y.H., Chang, J., Qin, L.D. Studying cancer stem cell dynamics on PDMS surfaces for microfluidics device design. *Sci. Rep*. **2013**, 3, 2332.

[17] Norman, L.L., Aranda-Espinoza, H. Cortical neuron outgrowth is insensitive to substrate stiffness. *Cell. Mol. Bioeng*. **2010**, 3, 398-414.

[18] Yang, L., van der Werf, K.O., Koopman, B., Subramaniam, V., Bennink, M.L., Kijkstra, P.J., Feijen, J. Micromechanical bending of single collagen fibrils using atomic force microscopy. . *J. Biomed. Mater. Res., Part A*. **2007**, 82: 160-168

[19] Gray, D.S., Tien,J., Chen, C.S. Repositioning of cells by mechanotaxis on surfaces with micropatterened Young's modulus. *J. Biomed. Mater. Res., Part A*. **2003**, 66A, 605-614.

[20] Graiver, D., Farminer, K.W., Narayan, R. A review of the fate and effects of silicones in the environment. *J. Polym. Environ*. **2003**, 11, 129-136

[21] Zheng, P and McCarthy T.J. Rediscovering silicons: molecularly smooth, low surface energy, unfiled, UV/Vis-transparent, extremely cross-linked, thermally stable, hard, elastic PDMS. *Langmuir*. **2010**, 26, 18585-90

[22] Jaeger, R.D.; Gleria, M. Silicones in medical applications. *Inorg. Polym*. Nova Science Publishers. **2007**.

[23] McDonald, J.C. and Whitesides, G.M. Poly(dimethylsiloxane) as a material for fabricating microfluidic devices. *Acc. Chem. Res*. **2002**, 35, 491-499

[24] Hoyle, C.E. and Bowman C.N. Thiol-ene click Chemistry. *Angew. Chem. Int. Ed.* **2010**, 49,1540-73

[25] Carlborg, C.F., Haraldsson T., Oberg, K., Malkoch, M., and Wijingaart, W. Beyond PDMS: off-stoichiometry thiol-ene (OSTE) based soft lithography for rapid prototyping of microfluidic devices. *Lab Chip*. **2011**, 11, 3136-3147

[26] Young, R.J. and Lovell P.A. Introduction to Polymers. Third Edition. CRC Press. **2011**. Print.

[27] Matyjaszewski, K., Davis, T.P. Handbook of radical polymerization. John Wiley & Sons, Inc. **2002**. Accessed online.

[28] Matisons, J., Marciniec, B. Hydrosilylation: A comprehensive review on recent advances. **2009** Vol.1. Chapter 1,5,6

[29] Wang, W. X. Preparation and surface pegylation of cross-linked polydimethylsiloxane substrates with tunable moduli. Dissertation, Mount Holyoke College, **2013**.

[30] Gillen, K.T.; Terrill, E.R.; Winter, R.M. Modulus mapping of rubbers using micro- and nano-indentation techniques. Rubber Chemistry and Technology. **2001**, 74, 428-450.

[31] Halliday, D.; Resnick, R.; Walker, J. Fundamentals of Physics, 5E, Extended. Wiley **1997**

[32] Sun, Y.; Akhremitchev, B.; Walker, G.C. Using the adhesive interaction between atomic force microscopy tips and polymer surfaces to measure the elastic modulus of compliant samples. *Langmuir.* **2004**, 20, 5837-5845.

[33] Notbohm, J.; Poon, B.; Ravichandran, G. Analysis of nanoindentation of soft materials with an atomic force microscope. *J. Mater. Res.* **2012**, 27, 229-237.

[34] Johnson, K.L.; Kendall, K.; Roberts, A.D. Surface energy and contact of elastic solids. *Proc London, Ser. A. Adv. Math. Phys*. **1971**, 324, 301-313

[35] Ebenstein, D.M. Nano-JKR force curve method overcomes challenges of surface detection and adhesion for nanoindentation of a compliant polymer in air and water. *J. Mater. Res*. **2011**, 26, 1026-1035.

[36] Ebenstein, D.M.; Wahl, K.J. A comparison of JKR-based methods to analyze quasi-static and dynamic indentation force curves. *J. Colliod Interface Sci*. **2006**, 298, 652-662.

[37] Kohn, J.C.; Ebenstein, D.M. Eliminating adhesion errors in nanoindentation of compliant polymers and hydrogels. *J. Mech. Behav. Biomed. Mater*. **2013**, 20, 316-326.

[38] Eaton, P., West, P. Atomic force microscopy. Oxford; New York: Oxford University Press, **2010**.

[39] Hertz, H. **1896**. Miscellaneous papers, p.146. London: Macmillan

[40] Pinto, S., Alves, P., Matos, C.M., Santos, A.C., Rodrigues, L.R., Teixeira, J.A., Gil, M.H. Poly(dimethyl siloxane) surface modification by low pressure plasma to improve its characteristics towards biomedical applications. *Colloids and Surfaces, B: Biointerfaces*. **2010**, 81, 20-26

[41] Wong, I., and Ho, C.M. Surface molecular property modifications for poly(dimehylsiloxane) (PDMS) based microfluidic devices. *Microfluid. Nanofluid.* **2009**, 7, 291-306

[42] Bacharouche, J.; Haidara, H.; Kunemann, P.; Vallat, M.; Roucoules, V. Singularities in hydrophobic recovery of plasma treated polydimethylsiloxane surfaces under non-contaminant atmosphere. *Sens. Actuators, A: Physical* **2013***, 197*, 25-29.

[43] Chumbimuni-Torres, K.Y., Coronado, R.E., Mfuh, A.M., Castro-Guerrero, C., Silva, M.F., Negrete, G.R., Bizios, R., and Garcia, C.D. Adsorption of proteins to thin-films of PDMS and its effect on the adhesion of human endothelial cells. *RSC Adv.* **2011**, 1, 706-714

[44] Young, T. An essay on the cohesion of fluids. *Phil. Trans. R. Soc. Lond.* **1805**, 95, 65-87.

[45] Yuan, Y. and Lee, T.R. Bracco, G (Eds)., Holst, B. (Eds). Contact angle and wetting properties. *Surface science techniques* **2013**, Chapter 1, 3-34

[46] Hollander, J.M., Jolly, W.L. X-Ray Photoelectron Spectroscopy. *Acc. Chem. Res.* **1970**, 3, 193-200

[47] Larsen, A.L., Sommer-Larsen, P., Hassager, O. Some experimental results for the end-linked polydimethylsiloxane network system. *E- Polym*. **2004**. 50, 1-18.

[48] Akagi, Y., Gong, J.P., Chung, U., and Sakai, T. Transition between phantom and affine network model observed in polymer gels with controlled network structure. *Macromolecules*. **2013**, 46, 1035-1040

[49] Lin, I-K; Ou,K.S., Liao, Y.M., Liu, Y., Chen, K.S., Zhang, X. Viscoelastic characterization and modeling of polymer transducers for biological applications, *J. of Microelectromech. Syst.* **2009**, 18, 1087-1099

[50] Pussak, D., Ponader, D., Mosca, S., Pompe, T., Hartmann, L., Schmidt, S. Specific adhesion of carbohydrate hydrogel particles in competition with multivalent inhibitors evaluated by AFM. *Langmuir.* **2014**, 30, 6142-6150

[51] Gerdelmann, J., Brunner, C., Pawlizak, S. Introduction: Scanning force microscopy (SPM), 2009. University of Leipzig Soft Matter Physics Division. http://www.unileipzig.de/~pwm/web/?section=introduction&page=sfm (accessed Nov. 26th, 2014)

[52] Bai, B.J. Using single-molecule imaging system combined with nano-fluidic chips to understand fluid flow in tight and shale gas formation. Missouri University of Science & Technology RPSEA. http://web.mst.edu/~baib/Shale%20Gas/RPSEA_ResearchCapability.html (accessed Nov. 26th, 2014)

[53] Rame-hart contact angle goniometers and tensiometers. Glossary of Surface Science Terms. http://www.ramehart.com/glossary.htm (accessed Nov. 26th, 2014)

[54] Stanford Engineering Nanoscale Prototyping Laboratory atomic force microscopy overview. http://npl-web.stanford.edu/archive/energy/atomic-force-microscope/ (accessed Nov. 27th, 2014)

[55] Smart, R., McIntyre, S., Bancroft, M., Bello, I. X-ray photoelectron spectroscopy. City University of Hong Kong, Surface Science Western, UWO. http://mmrc.caltech.edu/SS_XPS/XPS_PPT/XPS_Slides.pdf (accessed on Nov. 28th, 2014)

[56] Lowe, A.B. Thiol-ene "click" reactions and recent applications in polymer and materials synthesis. *Polym. Chem*. **2010**, 1, 17-36.